SHIP164 is a Chorein Motif Containing Lipid Transport Protein that Controls Membrane Dynamics and Traffic at the Endosome-Golgi Interface.

Michael G. Hanna[1-4*], Patreece Suen[2*], Yumei Wu[1-4], Karin M. Reinisch[2,6], Pietro De Camilli[1-6]

[1]Department of Neuroscience, Yale University School of Medicine, New Haven, Connecticut 06510, USA;

[2]Department of Cell Biology, Yale University School of Medicine, New Haven, Connecticut 06510, USA;

[3]Howard Hughes Medical Institute, Yale University School of Medicine, New Haven, Connecticut 06510, USA;

[4]Program in Cellular Neuroscience, Neurodegeneration and Repair, Yale University School of Medicine, New Haven, Connecticut 06510, USA;

[5]Kavli Institue for Neuroscience, Yale University School of Medicine, New Haven, Connecticut 06510, USA;

[6]Aligning Science Across Parkinson's (ASAP) Collaborative Research Network, Chevy Chase, MD.

* M. Hanna and P. Suen contributed equally to this paper.

Correspondence to Pietro De Camilli: pietro.decamilli@yale.edu and Karin M. Reinisch: karin.reinisch@yale.edu

ABSTRACT

Cellular membranes differ in protein and lipid composition as well as in the protein-lipid ratio. Thus, progression of membranous organelles along traffic routes requires mechanisms to control bilayer lipid chemistry and their abundance relative to proteins. The recent structural and functional characterization of VPS13-family proteins has suggested a mechanism through which lipids can be transferred in bulk from one membrane to another at membrane contact sites, and thus independently of vesicular traffic. Here we show that SHIP164 (UHRF1BP1L) shares structural and lipid transfer properties with these proteins and is localized on a subpopulation of vesicle clusters in the early endocytic pathway whose membrane cargo includes the cation-independent mannose-6-phosphate receptor (MPR) and ATG9. Loss of SHIP164 disrupts retrograde traffic of these organelles to the Golgi complex. Our findings raise the possibility that bulk transfer of lipids to endocytic membranes may play a role in their traffic.

INTRODUCTION

The homeostasis of intracellular membranes and their adaptation to changes in the functional state of the cell requires the coordination of protein and lipid transport. While much has been learned about protein traffic, less is known about the dynamics and transport of bilayer lipids. A significant fraction of such lipids move between organelles as part of the membranes of vesicular carriers. However, lipids also move via transport proteins that harbor them in hydrophobic cavities as they travel through the aqueous environment of the cytosol. This mode of transport has been known for decades, but has been increasingly appreciated over the last several years with the discovery of many new lipid transport proteins. Moreover, it has also become clear that many such proteins function at membrane contact sites, thus facilitating specificity and speed of lipid transport. Typically, these proteins contain modules or motifs that tether them to the two apposed membranes while lipid transfer modules move back and forth between them to extract and deliver lipids by a shuttling mechanism[1–5].

Recently, the characterization of VPS13 and its distant paralogue ATG2 has suggested a new mode of transport involving the flow of lipids along a protein bridge that connects the two membranes in eukaryotic cells[6–10]. A defining feature of these proteins is the presence of a conserved N-terminal region, ~125 residues long, referred to as the chorein-N motif[6,11–13]. In VPS13 and ATG2, this motif caps one end of an elongated rod (extended chorein domain). The rod comprises an extended ß-sheet that is highly curved to resemble a taco shell harboring a groove along its length[7,8]. A hydrophobic cavity in the chorein motif is continuous with the groove, whose floor is lined by hydrophobic amino acids, and so suited to accommodate many lipids at once and to allow their flow from one end of the rod to the other. In ATG2, the rod represents the bulk of the protein, while in VPS13 there are additional folded C-terminal domains that function in localization. Lipids are thought to flow unidirectionally along the rod, producing a net flow of lipids to the acceptor membrane and allowing for its expansion independent of contribution of new membrane lipids by vesicle fusion[9]. Accordingly, both the VPS13 paralogues and ATG2 have been implicated in membrane growth[14–17]. Many questions remain, however, about the precise mechanisms of action of these proteins. In some cases, the earliest stages of membrane growth mediated by VPS13 and ATG2 are characterized by the presence of clusters of small vesicles, raising questions about a potential interplay between the lipid transport properties of these proteins and vesicle fusion[14–16]. As studies of VPS13 have informed regarding ATG2 function and vice versa, characterization of other family members should yield further insights both as to how these proteins function and the cellular processes in which they participate.

A predicted chorein motif is present at the N-terminus of SHIP164 (also called UHRF1BP1L) and in its paralogue UHRF1BP1 (also called C6orf107), and fold prediction algorithms indicate high confidence that downstrem portions form an extended chorein domain ß-sheet[18,19] (**Figure 1A**). SHIP164 was first identified as an interactor of the Habc domain of Syntaxin 6 (Stx6) and shown to be a component of a multimolecular assembly including subunits of GARP[20]. GARP is a tethering complex which along with the structurally similar EARP cooperates with Stx6 in the fusion of endocytic vesicles with acceptor membranes in endosomes (EARP) and the Golgi complex (GARP)[21–23]. Moreover, over-expressed SHIP164-Stx6 complex was shown to colocalize with the cation-independent mannose-6-phosphate receptor (MPR) and to perturb the traffic of this receptor[20]. More recently, SHIP164 was identified as a top hit in a cellular-based screen for Rab5 effectors, further supporting a role of SHIP164 in the early endocytic pathway[24]. The possibility that SHIP164 may represent a lipid transport protein suggests that its characterization may reveal novel aspects of the biology of the endosomal system. Additional interest in this protein comes from its identification as a Parkinson's disease (PD) candidate gene from a large-

93 scale whole exome sequencing (WES) study[25]. To date, Nothing is known about the cell biology of
94 UHRF1BP1.
95
96 The goal of this study was to test the hypothesis that SHIP164 may be a lipid transport protein
97 and to gain new information into its localization and physiological function. Here we provide
98 direct evidence for a structural similarity of SHIP164 to ATG2 and the N-terminal half of VPS13
99 and for the property of SHIP164 to harbor and transport lipids. We show that SHIP64 localizes to
100 clusters of small vesicles in the endocytic pathway and demonstrate its importance in retrograde
101 traffic to the Golgi complex by both over-expression and loss-of-function studies. We also provide
102 evidence for a link between SHIP164 and ATG9A, raising the possibility that SHIP164, like ATG2,
103 may mediate lipid transport in partnership with ATG9A. Finally, our findings predict similar
104 properties for UHRF1BP1.
105
106 **RESULTS**
107
108 **Molecular properties of SHIP164 support a lipid transport function**
109
110 As a first step in assessing whether SHIP164 might function as a lipid transporter in the VPS13-
111 family, we assayed whether it can solubilize and transport lipids between membranes, and, if so,
112 which ones. We expressed full-length, N-terminally FLAG-tagged human SHIP164 (3xFLAG-
113 SHIP164) in Expi293 cells and purified it using anti-FLAG affinity resin, amid extensive washing
114 to remove non-specifically bound lipids, then analyzed the sample for co-purified molecules by
115 shotgun mass spectrometry lipidomics (**Figure 1B**). A large assortment of lipids, primarily
116 phospholipids, co-purified with SHIP164. There was no significant enrichment of a particular
117 phospholipid relative to the content of the whole cell, however.
118
119 The full-length construct was prone to aggregation, whereas constructs lacking a long predicted
120 unstructured segment (residues 901-1099) were soluble and were used in subsequent in vitro
121 studies. Further supporting that SHIP164 binds phospholipids, 3XFLAG-SHIP164$_{\Delta 901\text{-}1099}$ binds
122 nitrobenzoxadiazole (NBD)-labeled PE, co-migrating with this lipid on a native gel (**Figure 1C**).
123 From comparing the fluorescence that co-migrated with SHIP164 versus a well characterized lipid
124 transport module from the protein E-Syt2, we estimate that each SHIP164 molecule can
125 accommodate multiple lipids (~8), as might be expected if SHIP164 has an extended lipid binding
126 groove like VPS13 or ATG2[6,7].
127
128 We took advantage of the ability of SHIP164 to bind NBD-PE in designing an in vitro FRET-based
129 assay to monitor lipid transfer between membranes[6]. In this assay, SHIP164 is tethered (**Figure**
130 **1D**) between donor liposomes containing both rhodamine (Rh)- and NBD-labeled PE (61% DOPC,
131 30% PE, 2% NBD-PE, 2% Rh-PE, 5% Ni-NTA) and acceptor liposomes (65% DOPC, 30% PE, 5%
132 PI(4,5)P_2), initially lacking these fluorescent lipids. FRET between Rh and NBD reduces NBD
133 fluorescence initially. Transfer to acceptor liposomes and consequent dilution of the fluorescently
134 tagged lipids would reduce FRET and lead to increased NBD fluorescence. Consistent with a role
135 in lipid transfer, addition of SHIP164, but not of a an "empty" tether lacking a lipid transport
136 module, led to increased fluorescence (**Figure 1E**). Addition of SHIP164 to donor liposomes only,
137 in the absence of acceptor liposomes, led to a fast, smaller fluorescence increase due to the ability
138 of SHIP164 to extract lipids from the liposomes (**Fig. 1E, red arrow**), causing some dilution
139 (similar to observations for ATG2 and VPS13[6,7]). SHIP164 mediated fusion between donor and
140 acceptor liposomes would also lead to increased fluorescence. To discriminate between lipid
141 transfer (which occurs only between lipids in the outer leaflet of liposomes in the absence of
142 scramblases) and liposome fusion, we incubated donor and acceptor liposomes with and without
143 SHIP164, as before, then added dithionite to reduce NBD-labeled lipids exposed in the outer

leaflet. If SHIP164 had induced liposome fusion, the residual fluorescence after addition of SHIP164 would be higher than in its absence, as lipids in the internal leaflet would have been diluted[26]. In contrast, we found that the residual fluorescence after addition of dithionite was the same with and without addition of SHIP164 reflecting the fluorescence of lipids in the internal leaflet of donor liposomes that did not undergo dilution in the absence of membrane fusion (**Figure 1F**). These experiments support that SHIP164 can solubilize lipids and transfer them between membranes.

We next examined SHIP164 by electron microscopy. 2D class averages of negatively stained 3XFLAG-SHIP164$_{\Delta 901\text{-}1099}$ revealed a 200 Å long rod (**Figure 1G, Supplemental Figure 1A**). Comparison of SHIP164 with a MBP-SHIP164 fusion indicates that this rod represents a tail-to-tail dimer, as there are two densities corresponding to MBP, one at each end. The MBP-tag locates the SHIP164 N-terminus at the rod end. Whether this dimerization is physiologically relevant is unclear; for example, ATG2 similarily dimerizes in vitro, at high concentration, and in the absence of binding partners, but is thought to be monomeric in vivo[7]. Further characterization of 3XFLAG-SHIP164$_{\Delta 901\text{-}1099}$ using single particle cryo-electron microscopy techniques yielded a reconstruction at an estimated resolution of ~8.3 Å (**Supplemental Figure 1B&C**). As suggested by fold prediction algorithms (ref. [18,19])(see **Figure 1Ac-d**), a cavity runs along the entire length of the rod, as in VPS13 and ATG2 **(Figure 1 H&I)**. The algorithms also predict that this cavity is lined entirely with hydrophobic residues (**Figure 1Ac-d**). Thus, the cavity can accommodate the multiple lipids bound by SHIP164, and we propose that it could be a conduit for lipids to transit between membranes.

Collectively, these findings are consistent with the hypothesis that SHIP164 is a lipid transport protein. We next investigated its site of action within cells.

Localization of exogenous SHIP164 points to a role on endocytic organelles

Antibodies directed against SHIP164 did not yield a consistently reliable signal when tested by immunofluorescence. Thus, we examined the localization of exogenously tagged human SHIP164. In agreement with the study by Otto et al[20], SHIP164 tagged at the N-terminus (GFP-SHIP164) had a diffuse cytosolic localization when expressed in mammalian cell lines (e.g. HeLa, COS-7, RPE1) (**Supplemental Figure 2A**). As studies of VPS13 had shown that tags appended to the N-terminus (i.e the N-terminus of the chorein motif) interfere with its physiological function[6,27], we engineered tags at the C-terminus of SHIP164 (SHIP164-Halo) or at an internal site within the predicted disordered region (after amino acid residue 915; SHIP164^mScarlet-I) (**Figure 2A**) (ref. [6,27]). When either of these tagged SHIP164 constructs was expressed alone, punctate structures of varying size were observed throughout the cytoplasm, with the larger and brighter spots being localized in the central region of the cell, in proximity of the Golgi complex area (**Figure 2A**). Similar results were observed with other tags (Halo, GFP, mRFP, etc.) at either position. Conversely, even a small N-terminal tag appended to SHIP164^mScarlet-I (3xFLAG-SHIP164^mScarlet-I) abolished the presence of cytoplasmic foci (**Figure 2B**).

The scattered distribution of SHIP164^mScarlet-I foci throughout the cytosol combined with the results of Otto et al[20] suggesting a role of SHIP164 in the endocytic pathway, prompted us to examine the colocalization of SHIP164 relative to endosome markers. Many, but not all SHIP164 puncta, localized in proximity of spots or vacuoles positive for GFP-2xHrs^{FYVE}, a PI3P binding probe[28] (**Figure 2C**). Moreover, SHIP164^mScarlet-I spots were observed in close proximity to other co-expressed markers of endosome subcompartments, such as APPL1 (a very early, PI3P-negative endosomal station), WDFY2 (an endosomal station downstream of APPL1), and EEA1[29] (**Figure 2D**). SHIP164, however, did not localize on the organelles positive for these probes, but

195 on foci juxtaposed to them (**Figure 2C-E**). This was even more clear by observing
196 macropinosomes (both naturally occurring or induced by expressing constitutively active
197 Ras^{G12V}), given the large size of these vesicles[29] (**Supplemental Figure 2B**). As shown by live-
198 cell imaging, SHIP164 foci not only were variable in size as well as in fluorescence intensity, but
199 were also highly dynamic structures. They changed shape, often underwent fission, or coalesced
200 into larger spots although they tended to remain tethered to endosomes and micropinosomes
201 (**Figure 2F; Supplemental Movie 1**). In some cases, they were localized at sites where the
202 endosomes appeared to be close to the ER (**Figure 2E**), but were not restricted to the space
203 between these two organelles.
204
205 A more precise colocalization of exogenous SHIP164 was observed with Rab5 (BFP-Rab5b),
206 confirming previous results[20,24] (**Figure 2D**). In this case a pool of SHIP164 colocalized with Rab5
207 along the entire profile of vacuoles and, conversely, Rab5 robustly colocalized with the bright
208 SHIP164 foci closely apposed to large vacuoles (**Figure 2D**). This very strong colocalization
209 supports the hypothesis that SHIP164 is a Rab5 effector. However, expression of a dominant
210 negative Rab5 mutant (GFP-$Rab5a^{S34N}$) did not abolish bright SHIP164 (SHIP164-Halo) foci
211 suggesting that Rab5 is not necessary for their formation (**Supplemental Figure 2C**).
212
213 Notably, exogenous SHIP164 puncta colocalized with endogenous cation-independent mannose-
214 6-phosphate receptor (MPR) (as detected by immunofluorescence) and its expression (leading to
215 higher than normal levels of SHIP164) also resulted in an alteration of the localization of the MPR,
216 which accumulated in large foci where the two proteins colocalized (**Figure 2G**). These
217 accumulations occurred throughout the cell but were especially large in proximity of the Golgi
218 complex, where the normal Trans-Golgi Network (TGN)-like appearance of MPR was replaced by
219 these large accumulations located at some distance from GM130, a Golgi complex marker[30] (see
220 **Figure 2G** for COS-7 cells and **Supplemental Figure 2D** for HeLa cells). A similar
221 redistribution of MPR and also of the Golgi/endosome protein sortilin[31] was observed in RPE1
222 (retinal pigment epithelial) cells transfected with a polycistronic expression plasmid encoding
223 untagged SHIP164 and a soluble RFP to confirm transfection, ruling out non-specific effects of
224 the engineered fluorescent tag of exogenous SHIP164 (**Figure H&I; Supplemental Figure**
225 **2E&F**). Such changes were not observed with TGN46, another protein enriched in the TGN that
226 cycles to and from the plasma membrane and endosomes[21,32,33] (**Supplemental Figure 2G&H**).
227 This difference is in line with the known traffic of MPR and sortilin versus TGN46 in different
228 vesicular carriers[33,34] (see also below).
229
230 **Foci of exogenous SHIP164 reflect accumulations of small vesicles**
231
232 To gain further insight into the precise nature of foci of over-expressed SHIP164, we performed
233 correlative light-electron microscopy (CLEM) of COS-7 cells co-expressing the early endosome
234 marker GFP-WDFY2 and SHIP164^mScarlet-I (**Figure 3A**). Both conventional EM and FIB-
235 SEM were performed. We again employed Ras^{G12V} to induce the formation of macropinosomes[35]
236 to facilitate the alignment of fluorescence and EM images. This analysis revealed that spots of
237 SHIP164 fluorescence reflected accumulations of 100's of tightly packed approximately 50-60 nm
238 vesicles juxtaposed to endosomal membranes positive for GFP-WDFY2 (**Figure 3A**). An
239 approximately 70nm thick matrix appeared to anchor these clusters to the WDFY2-positive
240 vacuoles and the space occupied by this matrix was nearly devoid of vesicles (**Figure 3A&C**). ER
241 tubules were present in proximity of these clusters and often penetrated them, but there did not
242 seem to be sites of preferential accumulation of vesicles (**Figure 3B**). The appearance of these
243 vesicle accumulations and their dynamic nature revealed by live imaging (see above) was
244 reminiscent of other vesicle clusters, such as synaptic vesicles clusters in nerve terminals, recently
245 shown to be organized according to principles of liquid-liquid phase separation[36–38]. As such

246 "phases" often involve low affinity interaction of disordered protein regions[39], we considered the
247 possibility that the "disordered region" of SHIP164 (see **Figure 1Ac**) may be responsible for their
248 formation. However, a truncated form of SHIP164 ($SHIP164_{1-873}$-mRFP) that lacks the disordered
249 region also induced the formation of large fluorescence puncta closely juxtaposed to endosomes
250 (**Supplemental Figure 3**). Thus, the mechanism responsible for the clustering of SHIP164
251 positive vesicles remains unclear. Also unclear is how such clusters are anchored to the large
252 vacuoles.
253
254 As these vesicle accumulations, which to our knowledge were never observed in WT cells,
255 suggested an abnormal effect of over-expressed SHIP164, we next tagged SHIP164 at the
256 endogenous locus to assess its localization when expressed at the endogenous level.
257
258 **Endogenous SHIP164 localizes to small clusters of vesicles near the cell edge**
259
260 We tagged SHIP164 at the endogenous locus in HeLa cells. Specifically, we engineered a
261 mNeonGreen (mNG) tag in the disordered region after amino acid residue 1092 via the ORANGE
262 genomic editing method[40] (**Figure 4A**). Two clones were isolated where expression of
263 endogenous SHIP164^mNG (eSHIP164^mNG) was confirmed by the presence of a band running
264 at the appropriate molecular weight and recognized by western blotting with both anti-SHIP164
265 and anti-mNeonGreen antibodies (**Figure4B**). Correct insertion of the tag was validated by DNA
266 sequencing of the targeted gene region (**Figure 4C**).
267
268 Like exogenous SHIP164, eSHIP164^mNG had a punctate appearance. However,
269 eSHIP164^mNG puncta were very much smaller and, in contrast to foci of over-expressed
270 SHIP164 (**Figure 2A**), were primarily localized at the cell edge (**Figure 4D**). On the other hand,
271 when SHIP164^mScarlet-I was expressed in these endogenously tagged cells, exogenous
272 mScarlet-I and endogenous mNeonGreen fluorescence precisely overlapped in large foci,
273 including the ones localized in deep regions of the cell (**Supplemental Figure 4A**). This
274 demonstrates that endogenous and exogenous SHIP164 completely intermix—as expected from
275 correct gene targeting—confirming that large foci are the result of SHIP164 over-expression.
276
277 To determine whether puncta of eSHIP164^mNG represent MPR positive vesicles, we generated
278 a double knock-in (DKI) HeLa cell line where both SHIP164 and MPR were tagged at their
279 endogenous loci (eSHIP164^mNG and eMPR-mScarlet-I). Most, but not all, eSHIP164^mNG
280 positive puncta colocalized and moved together with puncta of eMPR-mScarlet-I fluorescence
281 (**Figure 4E; Supplemental Movie 2**). Conversely, many eMPR-mScarlet-I puncta at the edge
282 of the cell colocalized and moved together with puncta of eSHIP164^mNG (**Figure 4E**), while
283 MPR vesicles located deeper into the cell were negative for SHIP164[41,42]. Fluorescent puncta
284 positive for the two proteins were distinct from vesicles positive for newly internalized labeled
285 EGF (EGF-647) revealing that endogenous SHIP164 localizes to a specific endocytic
286 subpopulation (**Supplemental Figure 4B**). Interestingly, an intrinsic membrane protein of
287 unknown function, that is listed as a SHIP164 interactor in BioGRID (https://thebiogrid.org),
288 FAM174a, strikingly colocalized with exogenous SHIP164 accumulations, although FAM174a was
289 also present in the Golgi complex and other compartments of the secretory/endocytic pathways
290 (**Supplemental Figure 4C&D)**.
291
292 To gain further insight into the nature of endogenous SHIP164 puncta, we again employed CLEM
293 in eSHIP164^mNG HeLa cells also expressing a marker of mitochondria (mito-BFP) to aid in
294 fluorescence and EM image alignment (**Figure 4F**). Given the small size of the fluorescent
295 structures, FIB-SEM rather than TEM was used in spite of the lower resolution afforded by FIB-
296 SEM as this technique allows a better alignment between fluorescence and EM images in 3D. This

297 analysis revealed that, similar to the large fluorescence puncta of exogenously expressed SHIP164,
298 spots of eSHIP164^mNG fluorescence reflected tightly packed clusters of small vesicles and short
299 tubules (**Figure 4F&G**). However, these clusters were much smaller (10's instead of 100's of
300 vesicular structures). As revealed by 3D reconstruction of FIB-SEM volumes (**Figure 4G**) and by
301 fluorescence of cells also expressing the ER marker RFP-Sec61 (**Figure 4H**), ER tubules were
302 localized in close proximity of these clusters but vesicles were preferentially associated with
303 themselves rather than with the ER.
304
305 Collectively, these findings indicate that SHIP164, when expressed at endogenous levels, is
306 selectively localized on small MPR-positive vesicles near the cell periphery. They further imply
307 that SHIP164 dissociates from such vesicles as they travel to deeper cellular regions and that the
308 presence of exogenous SHIP164 on the very large vesicle clusters in central cell regions near the
309 Golgi complex reflect an over-expression defect. To better understand SHIP164's dynamics in the
310 endocytic pathway we investigated its interactions.
311
312 **Interaction of SHIP164 with proteins implicated in the targeting of endocytic**
313 **cargoes to the Golgi complex.**
314
315 We confirmed the previously reported colocalization of exogenous SHIP164 with over-expressed
316 Stx6[20] (**Figure 5A**). SHIP164 and Stx6 colocalized on spots scattered throughout the cytoplasm
317 and in the Golgi complex area irrespective of the presence or absence of N-terminal tags, i.e. tags
318 that impair the localization of SHIP164 to vesicles enriched foci when expressed alone
319 (**Supplemental Figure 2A**). This indicates that binding to Stx6 does not play a major role in
320 the localizations of SHIP164 described above.
321
322 The location of the Stx6 binding site within the SHIP164 protein was not known. A short
323 hydrophobic motif ($L_{37}xxYY_{41}$) responsible for binding to the Habc domain of Stx6 was previously
324 identified in the N-terminal region of VPS51[23]. A similar motif ($L_{759}xxYY_{763}$) is present in a
325 predicted disordered loop of SHIP164 within the extended chorein domain (**Figure 5E; Figure**
326 **1Ac**) and mutations of both tyrosine resides (Y772A, Y773A) abolished the recruitment of GFP-
327 SHIP164 (GFP-SHIP164$^{Y772A, Y773A}$; i.e. N-terminally tagged SHIP164 that when expressed by itself
328 is cytosolic) to mRFP-Stx6 (**Supplemental Figure 5A**). However, the same mutations, when
329 introduced into C-terminally tagged SHIP164 (SHIP164$^{Y772A, Y773A}$-mRFP) did not affect the
330 localization of the protein into bright foci in cells not transfected with Stx6, further indicating that
331 Stx6 does not account for these localizations (**Supplemental Figure 5B**).
332
333 To identify additional SHIP164 interacting partners that may impact its localization and/or
334 function, we performed pull-down experiments from detergent solubilized mouse brain lysates
335 onto purified SHIP164 (3xFLAG-SHIP164) bound to anti-FLAG resin. Shotgun mass
336 spectrometry of the affinity-purified material showed a significant specific enrichment (relative
337 to control) of the light chains 1 and 2 (DYNLL1/2; also known as LC8) of cytoplasmic dynein, the
338 minus-end directed microtubule motor[43] (**Figure 5B**). DYNLL1/2 act as dynein complex
339 adaptors which mediate a wide variety of protein-protein interactions through a short linear
340 binding motif[44] ($V_{-5}[S/N/T]_{-4}[K/R]_{-3}X_{-2}T_{-1}Q_0T_{+1}$). Accordingly, a motif that fits this consensus is
341 present in SHIP164 near its C-terminus ($V_{1395}TQATQT_{1401}$) and LC8 is another protein listed
342 among putative SHIP164 interactors in BioGRID (**Figure 5E**). Moreover, when an MBP-tagged
343 fragment of SHIP164 containing this region (MBP-SHIP164$_{1312-1464}$) and untagged LC8 were co-
344 expressed in bacteria from a polycistronic plasmid, LC8 co-purified with MBP-SHIP164$_{1312-1464}$ on
345 amylose-resin and co-fractionated with MBP-SHIP164$_{1312-1464}$ when the eluate of the resin was
346 fractionated on a size-exclusion column indicating a direct interaction (**Figure 5C**).
347

348 Interestingly, another potential SHIP164 interactor listed in BioGRID, Rab45 (RASEF), is linked
349 to dynein function. Rab45 and its better-characterized paralog CRACR2a are dynein/dynactin
350 activators that connect endocytic cargoes to minus-end microtubule transport[45,46]. In agreement
351 with the possibility that SHIP164 may be an effector of Rab45, over-expression of Rab45
352 dramatically concentrated both transfected SHIP164^mScarlet-I and endogenously tagged
353 SHIP164 (eSHIP164^mNG) to perinuclear spots (i.e. the position occupied by the centrosome),
354 depleting them from the periphery (**Figure 5D; Supplemental Figure 5C**). At this perinuclear
355 location, SHIP164 and Rab45 precisely colocalized (**Figure 5D; Supplemental Figure 5C**).
356 Over-expression of Rab45 also clustered endogenous MPR tagged at the C-terminus with a
357 mNeonGreen tag (eMPR-mNeonGreen), but only in cells over-expressing SHIP64, i.e. in cells
358 where the majority of MPR-positive vesicles (not only the peripheral vesicles) are positive for
359 SHIP164 (**Supplemental Figure 5D**). A dominant-inactive Rab45 (S555N) mutant had a
360 cytosolic localization did not induce SHIP164 accumulation in this area suggesting that the
361 nucleotide bound state of Rab45 regulates recruitment (**Supplemental Figure 5E**).
362
363 Taken together, our interaction studies point to an association of SHIP164 with vesicles that traffic
364 from the cell periphery to the centrosomal/Golgi complex region, although endogenous SHIP164
365 appears to be shed by vesicles as they move to central regions of the cells unless Rab45 is over-
366 expressed. One would therefore expect a role of SHIP164 in some aspect of retrograde membrane
367 traffic. To validate this hypothesis, we performed loss-of-function studies.
368
369 **Defects in retrograde membrane traffic to the TGN in SHIP164 knockout cells**
370
371 To assess the impact of the absence of SHIP164 on cell physiology we chose RPE1 cells as a model
372 system due to their reliable genetic editing and flat morphology optimal for organelle imaging.
373 Using CRISPR/Cas9 methodology, two independent SHIP164 knockout (KO) clones were
374 generated where indels led to a frameshift of the reading frame that resulted in premature stop
375 codons as shown by sequencing (**Supplemental Figure 6A**). In both clones, identical indels
376 were observed on both alleles (but different between the two clones) and absence of the SHIP164
377 protein was confirmed by western blotting (**Figure 6A**). No obvious changes were observed in
378 cell shape, in mitochondria, ER, or Golgi morphology as assessed by the cis-Golgi marker
379 (GM130) (see below). Two differences, however, were noted.
380
381 One was a difference in the size of endosomes labeled by EEA1 (visualized by immunostaining),
382 and GFP-2xHrs^{FYVE} (visualized by live-cell imaging) as the largest (>1 μm^2) vesicles positive for
383 these markers in WT cells were mostly absent in KO cells (**Figures 6B-C,** **, $p<0.01$).
384
385 The other difference was a change in the steady state localization of MPR and other proteins that
386 recycle between the cell periphery (plasma membrane and endosomes) and the TGN. Specifically,
387 upon immunostaining of SHIP164 KO cells for the MPR, an increase in the pool of MPR localized
388 in vesicles scattered throughout the cytoplasm relative to the pool localized in the Golgi complex
389 area was observed[42], (**Figure 6D,** **, $p<0.01$). The localizations by immunofluorescence of
390 TGN46 and of Sortilin showed a similar difference relative to controls (**Figure 6E &**
391 **Supplemental Figure B,** **, $p<0.01$), although the vesicles positive for TGN46 were different
392 from those positive for MPR and sortilin (**Supplemental Figure 6C**). As a control, the ratio of
393 clathrin heavy chain (CHC) immunoreactivity sparse throughout the cytoplasm relative to
394 immunoreactivity in the Golgi complex was also measured and such ratio was not statistically
395 different between SHIP164 KO cells and parental control cells (**Figure 6F**).
396
397 To validate the dependence of these phenotypes from the lack of SHIP164, we attempted to rescue
398 them by expressing exogenous SHIP164 in the KO cells. To this aim we used the polycistronic

399 construct described above encoding both untagged SHIP164, in order to avoid any artifact due to
400 the tag, and soluble RFP, to identify transfected cells. In both KO clones, transfection of this
401 construct (likely resulting in levels of SHIP164 higher than in WT cells), but not of a construct
402 encoding only the RFP reporter, resulted in the rescue of the vesicles-to-Golgi ratio of TGN46
403 immunoreactivity (**Figure 6G**; *, $p<0.05$; **, $p<0.01$). However, in the case of MPR and sortilin,
404 expression of the SHIP164 construct did not restore their WT localization, but resulted in their
405 robust accumulation into large foci as shown above upon SHIP164 over-expression in wild type
406 cells (**Supplemental Figure 6D**). This result is most likely explained by the disrupting effect of
407 SHIP164 over-expression, which, as shown above, does not impact TGN46 localization
408 (**Supplemental Figure 2G&H**). Likewise, SHIP164 over-expression did not seem to rescue the
409 presence of the large EEA1 positive endosomes present in WT cells as it induced large focal EEA1
410 accumultions, but these did not have the typical vacuolar apperance. (**Supplemental Figure
411 6E**). Also in this case this result may be to due a dominant negative effect as similar EEA1 positive
412 clusters rather than the typical vacuolar structures were observed in WT cells over-expressing
413 SHIP164 (**Supplemental Figure 6E**). However, we confirmed the impact of SHIP164
414 deficiency on the presence of large EEA1 endosomes by SHIP164 siRNA-dependent knockdown
415 in RPE-1 cells, thus ruling out off-target effects of CRISPR/Cas9 editing (**Supplemental Figure
416 6F&G**; **, $p<0.01$).
417
418 We conclude that loss of SHIP164 function may globally impact membrane traffic between the
419 cell periphery and the Golgi complex, while over-expression of SHIP164 disrupts selectively the
420 retrograde traffic of a subset of the vesicles with which SHIP164 is associated.
421
422 **Presence of ATG9A in clusters of SHIP164-positive vesicles**
423
424 The structural similarity of SHIP164 to proteins thought to mediate bulk lipid transport—
425 particularly ATG2—suggests a similar function of SHIP164[6,7,11,47]. A plausible scenario is that
426 SHIP164 may allow the regulation of bilayer lipids (abundance and possibly also type of lipids)
427 on organelles of the endocytic pathway by mediating transient contacts with these organelles and
428 either the ER or other membranes to transport lipids[4,9]. The lack of the large endosomes in
429 SHIP164 KO cells would be consistent with a role of SHIP164 in bulk transfer of lipids. So far,
430 however, we have not found direct evidence for a role of SHIP164 as a tether between two
431 membranes. Moreover, as stated above, the endosomal size phenotype could not be clearly
432 rescued by the expression of exogenous SHIP164 in SHIP164 KO cells (**Supplemental Figure
433 6E**), thus preventing us from directly testing this hypothesis using SHIP164 proteins that cannot
434 transport lipids, in addition to a propensity to aggregate in living cells of putative lipid-transport
435 dead mutants that we generated.
436
437 ATG2 was found to function in cooperation with the scramblase ATG9, as lipids are delivered by
438 ATG2 to the cytosolic leaflet of the receiving membrane and thus lipid scrambling is needed to
439 allow equilibration of lipid concentration on both bilayer leaflets[10,48–51]. In WT cells, ATG9
440 (ATG9A) is concentrated in the Golgi complex area and also present as scattered dots throughout
441 the cytoplasm (**Figure 7A).** Interestingly, we found that ATG9A-GFP is highly concentrated on
442 the SHIP164 positive foci resulting from SHIP164 over-expression (**Figure 7B**). Moreover, while
443 no major redistribution of ATG9A-GFP is observed in cells over-expressing Rab45 (RFP-Rab45),
444 co-expression of SHIP164-Halo with RFP-Rab45 resulted in a striking co-enrichment and
445 colocalization of all three proteins in the centrosomal area proving that ATG9A is localized on
446 SHIP164-positive vesicles (**Figure 7C**). We also explored whether autophagy was affected in
447 SHIP164 KO cells, but we did not find any effect on LC3 abundance upon starvation. While the
448 localization of ATG9A on SHIP164 positive vesicles does not provide evidence for a lipid transport

activity of SHIP164, it is consistent with such an activity and raises the interesting possibility that ATG9A may have more general functions in cell physiology than a selective role in autophagy[52].

UHRF1BP1, a SHIP164 paralogue, is also localized in the endocytic pathway

UHRF1BP1 shares substantial primary sequence similarity (42% identity) and domain organization with SHIP164[20]. Accordingly, phenotypes produced by expression of exogeneous UHRF1BP1 (UHRF1BP1-Halo) revealed similarities to those produced by the expression of exogenous SHIP164. As in the case of SHIP164, UHRF1BP1-Halo localized to foci of varying size and fluorescence intensity with the larger foci being concentrated in the central region of the cell (**Figure 7D**). These foci were positive for exogenous ATG9A (ATG9A-GFP) (**Figure 7E**). However, in contrast to SHIP164 foci, which were primarily associated with early endosomes, UHRF1BP1 foci were predominantly associated with LAMP1-GFP-positive organelles, in agreement with previous work suggesting that UHRF1BP1 is a Rab7 effector, rather then a Rab5 effector[24] (**Supplemental Figure 7**). We conclude that SHIP164 and UHRF1BP1 likely function in a similar manner but at different stations of the endocytic pathway

DISCUSSION

Our study identifies SHIP164 as a bona fide member of the chorein motif protein family with a role in membrane traffic. The EM-analyses of SHIP164 show that as in VPS13 and ATG2, the two well established members of this family, the N-terminal chorein motif of SHIP164 caps an extended rod that harbors a cavity running along its length[6–8,47]. Fold prediction algorithms (Alphafold, trRosetta) indicate that SHIP164 features an extended ß-sheet that resembles a taco shell, whose concave elongated surface is lined with hydrophobic residues, and so constitutes a groove that can solubilize multiple lipids[18,19]. In vitro lipid binding and transfer assays further support that SHIP164 might function as a lipid transfer protein. The SHIP164 paralogue UHRF1BP1 is predicted to have a similar structure.

Our analysis of the subcellular localization of SHIP164 reveals an association with endocytic organelles, extending previous observations[20,24]. This is supported by several pieces of evidence: 1) Endogenous SHIP164 is predominantly localized on a population of small peripheral vesicles that assemble in small clusters and contain in their membranes endosomal cargo proteins, such as MPR[42]. 2) Over-expressed SHIP164 drastically enlarges the size of these clusters, which become, in many cases, tightly associated with vacuoles positive for markers of early endosomal subcompartments, such as Rab5, APPL1, WDFY2, PI3P, and EEA1 and are found also in deep regions of the cell. 3) The interactors of SHIP164 that we have identified or validated are endocytic factors or proteins that mediate retrograde organelle traffic from the cell periphery to the centrosomal/Golgi complex area. One of them is Rab5, an early endosomal Rab[53]. Another one is Stx6, a component of SNARE complexes that mediates the fusion of vesicles with recycling endosomes and with the Golgi complex and whose action is facilitated by the GARP and EARP tethering complexes[54–56]. Interestingly, binding of SHIP164 to the Habc domain of Stx6 is mediated by the same motif used by the GARP and EARP subunit VPS51, also a Stx6 interactor[21,23]. While this finding implies a competitive binding to Stx6, it also suggests an interplay of SHIP164 with GARP, further linking SHIP164 to retrograde traffic. A third interactor is the light chain of dynein (DYNLL1/2), the microtubule motor that mediates retrograde traffic[57]. The fourth is Rab45, an unconventional Rab that anchors endocytic vesicles to dynein, creating an additional link to dynein and retrograde traffic[45,46]. Notably, however, SHIP164, when expressed at endogenous levels is predominantly associated with peripheral vesicles, suggesting a regulated interaction with vesicles that is lost and replaced by other interactors as they travel to deeper destinations in the cell.

A role of SHIP164 in retrograde traffic is further supported by SHIP164 loss of function and gain-of-function studies. In SHIP164 KO cells, a larger pool of proteins that shuttle between the cell periphery and the Golgi complex (MPR, sortilin and TGN46) is localized on vesicles scattered throughout the cytoplasm relative to their major pool localized in the Golgi complex area suggesting a defect in transport/docking or fusion with the Golgi complex. Similar observations have been made in cells deficient in GARP function[21,58,59]. Conversely, SHIP164 over-expression (gain-of-function) results in large vesicle clusters positive for MPR and sortilin, but not for TGN46, indicating that loss-of-function and gain-of-function effects are not precise opposites. A potential scenario is that the accumulation of sortilin and MPR vesicles results from a block in their progression to the next traffic station produced by excess SHIP164. Such dominant negative effect could be the result of sequestration of, or competition with, critical factor(s) (for example GARP) by over-expressed SHIP164 or by alteration of membrane lipid homeostasis.

A key question is how the structure and molecular properties of SHIP164, which predict a lipid transport function at intracellular membrane contact sites, similar to the proposed function of VPS13 and ATG2, relates to the observed localization and loss-of-function phenotypes of SHIP164. We consider the hypothesis that SHIP164, as proposed for VPS13 and ATG2, may function in the transport of lipids from one membrane where the chorein domain may extract lipids – for example the ER – to other membranes[9] and more specifically to the small vesicles enriched with endogenous SHIP164. This transport may deliver specific lipids or simply be responsible for membrane expansion. However, the localization of SHIP164 that we have observed is not at contacts of two types of membranous organelles, as predicted by this model. While some SHIP164 foci detectable by fluorescence appear to be localized at the interface of the ER and endosomes, such foci are represented by vesicle clusters and not by SHIP164 tethers between the ER and endosomes. Moreover, until now we have not identified the binding of SHIP164 to any ER protein. SHIP164 does not have an FFAT or FFAT-like motif that, as in the case of VPS13[6,60], could account for binding to the ER protein VAP[61,62]. In spite of these considerations, binding of SHIP164 to the ER cannot be excluded. Binding to the ER of SHIP164 tagged at the endogenous locus is difficult to analyze given the small size of SHIP164 associated vesicles. SHIP164 over-expression may overwhelm a binding site on the ER, unless such binding site was also over-expressed. One should also consider that an interaction with the ER of SHIP164-positive transport vesicles may be regulated and only transient.

Of special interest in the context of protein-mediated lipid transport is the strong colocalization of SHIP64 with ATG9A, as ATG9A is a functional partner of ATG2 in the expansion of the autophagic membrane[48–50,63]. ATG9A, a protein scramblase, is thought to allow equilibration between the two bilayer leaflets, as phospholipids are delivered to the cytosolic leaflet of the autophagic membrane by ATG2[48–50]. While ATG9A was discovered as a core component of the autophagy machinery, it is plausible that it may function in other contexts, as also recently reported[52], more so in cooperation with a protein that shares strong similarities with ATG2, such as SHIP164. Interestingly, studies of ATG9A have consistently localized it to small vesicles often organized in clusters, similar to the SHIP164 vesicles described here[16,64]. Thus, the overlapping localization of SHIP164 and ATG9A is consistent with a role of SHIP164 in lipid transport. The absence of large endosomes in SHIP164 KO cells would be supportive of a role of SHIP164 in lipid transfer to expand the membranes of endocytic organelles, but since this phenotype could not be clearly rescued (possibly due to dominant negative effects of SHIP164 overexpression), its significance remains uncertain. Future studies will be needed to provide further mechanistic insight into these findings. We note that mechanisms to control bulk lipid transport to the membrane of an endocytic organelle independent of membrane fusion may help fine tune the

protein/lipid ratio of such membrane and may therefore play an important role in controlling its maturation as it travels to deeper positions in the cell.

Finally, in view of the link between the function of SHIP164 and GARP suggested by our study and a previous study[20], it is of interest that defects in retrograde traffic from the cell periphery to the Golgi complex produced by SHIP164 loss-of-function have similarities to those observed upon loss of function of the GARP complex[20,58]. GARP has also been linked to lipid metabolism. In zebrafish, loss of the GARP subunit fat-free (Ffr) (later identified as the paralog to mammalian VPS51) results in a striking defect of the absorption into the body of dietary lipids[65]. Defects in GARP in mice or humans, either at the cellular or organismal level, result in abnormal sphingolipid metabolism (with an abnormal accumulation of long chain bases) and neurodegenerative conditions[59,66,67]. SHIP164 was reported be a Parkinson's disease candidate gene[25] and loss-of-function mutations in VPS13C, another chorein motif lipid transport protein implicated in the endocytic/lysosome pathway is responsible for familial forms of Parkinson's disease[68]. It is therefore possible that SHIP164 may be part of a network of proteins that play an important role in neuronal health by controlling lipid transport and metabolism at the interface with membrane traffic.

568 **REFERENCES**

569 1. Alva, V. & Lupas, A. N. The TULIP superfamily of eukaryotic lipid-binding proteins as a
570 mediator of lipid sensing and transport. *Biochimica et Biophysica Acta (BBA) - Molecular*
571 *and Cell Biology of Lipids* **1861,** 913–923 (2016).
572 2. Prinz, W. A., Toulmay, A. & Balla, T. The functional universe of membrane contact sites.
573 *Nature Reviews Molecular Cell Biology* **21,** 7–24 (2020).
574 3. Saheki, Y. & Camilli, P. D. Endoplasmic Reticulum-Plasma Membrane Contact Sites.
575 *Annual review of biochemistry* **86,** 659–684 (2017).
576 4. Reinisch, K. M. & Prinz, W. A. Mechanisms of nonvesicular lipid transport. *Journal of*
577 *Cell Biology* **220,** (2021).
578 5. Wong, L. H., Gatta, A. T. & Levine, T. P. Lipid transfer proteins: the lipid commute via
579 shuttles, bridges and tubes. *Nature Reviews Molecular Cell Biology* **20,** 85–101 (2019).
580 6. Kumar, N., Leonzino, M., Hancock-Cerutti, W., Horenkamp, F. A., Li, P. Q., Lees, J. A.,
581 Wheeler, H., Reinisch, K. M. & De Camilli, P. VPS13A and VPS13C are lipid transport proteins
582 differentially localized at ER contact sites. *The Journal of cell biology* (2018).
583 7. Valverde, D. P., Yu, S., Boggavarapu, V., Kumar, N., Lees, J. A., Walz, T., Reinisch, K. M.
584 & Melia, T. J. ATG2 transports lipids to promote autophagosome biogenesis. *The Journal of*
585 *cell biology* **14,** jcb.201811139 (2019).
586 8. Li, P., Lees, J. A., Lusk, C. P. & Reinisch, K. M. Cryo-EM reconstruction of a VPS13
587 fragment reveals a long groove to channel lipids between membranes. *The Journal of cell*
588 *biology* **219,** (2020).
589 9. Leonzino, M., Reinisch, K. M. & De Camilli, P. Insights into VPS13 properties and
590 function reveal a new mechanism of eukaryotic lipid transport. *Biochim Biophys Acta Mol*
591 *Cell Biol Lipids* **1866,** 159003 (2021).
592 10. Noda, N. N. Atg2 and Atg9: Intermembrane and interleaflet lipid transporters driving
593 autophagy. *Biochimica et Biophysica Acta (BBA) - Molecular and Cell Biology of Lipids*
594 **1866,** 158956 (2021).
595 11. Osawa, T., Kotani, T., Kawaoka, T., Hirata, E., Suzuki, K., Nakatogawa, H., Ohsumi, Y. &
596 Noda, N. N. Atg2 mediates direct lipid transfer between membranes for autophagosome
597 formation. *Nat Struct Mol Biol* **26,** 281–288 (2019).
598 12. Ueno, S., Maruki, Y., Nakamura, M., Tomemori, Y., Kamae, K., Tanabe, H., Yamashita,
599 Y., Matsuda, S., Kaneko, S. & Sano, A. The gene encoding a newly discovered protein, chorein,
600 is mutated in chorea-acanthocytosis. *Nat Genet* **28,** 121–122 (2001).
601 13. Rampoldi, L., Dobson-Stone, C., Rubio, J. P., Danek, A., Chalmers, R. M., Wood, N. W.,
602 Verellen, C., Ferrer, X., Malandrini, A., Fabrizi, G. M., Brown, R., Vance, J., Pericak-Vance,
603 M., Rudolf, G., Carrè, S., Alonso, E., Manfredi, M., Németh, A. H. & Monaco, A. P. A
604 conserved sorting-associated protein is mutant in chorea-acanthocytosis. *Nat Genet* **28,** 119–
605 120 (2001).
606 14. Park, J.-S., Okumura, Y., Tachikawa, H. & Neiman, A. M. SPO71 Encodes a
607 Developmental Stage-Specific Partner for Vps13 in Saccharomyces cerevisiae. *Eukaryotic Cell*
608 **12,** 1530–1537 (2013).
609 15. Da Costa, R., Bordessoules, M., Guilleman, M., Carmignac, V., Lhussiez, V., Courot, H.,
610 Bataille, A., Chlémaire, A., Bruno, C., Fauque, P., Thauvin, C., Faivre, L. & Duplomb, L.
611 Vps13b is required for acrosome biogenesis through functions in Golgi dynamic and
612 membrane trafficking. *Cell. Mol. Life Sci.* **77,** 511–529 (2020).
613 16. Mari, M., Griffith, J., Rieter, E., Krishnappa, L., Klionsky, D. J. & Reggiori, F. An Atg9-
614 containing compartment that functions in the early steps of autophagosome biogenesis.
615 *Journal of Cell Biology* **190,** 1005–1022 (2010).
616 17. Chang, C., Jensen, L. E. & Hurley, J. H. Autophagosome biogenesis comes out of the
617 black box. *Nat Cell Biol* **23,** 450–456 (2021).

618 18. Jumper, J., Evans, R., Pritzel, A., Green, T., Figurnov, M., Ronneberger, O.,
619 Tunyasuvunakool, K., Bates, R., Žídek, A., Potapenko, A., Bridgland, A., Meyer, C., Kohl, S. A.
620 A., Ballard, A. J., Cowie, A., Romera-Paredes, B., Nikolov, S., Jain, R., Adler, J., Back, T.,
621 Petersen, S., Reiman, D., Clancy, E., Zielinski, M., Steinegger, M., Pacholska, M.,
622 Berghammer, T., Bodenstein, S., Silver, D., Vinyals, O., Senior, A. W., Kavukcuoglu, K., Kohli,
623 P. & Hassabis, D. Highly accurate protein structure prediction with AlphaFold. *Nature* **596,**
624 583–589 (2021).
625 19. Yang, J., Anishchenko, I., Park, H., Peng, Z., Ovchinnikov, S. & Baker, D. Improved
626 protein structure prediction using predicted interresidue orientations. *PNAS* **117,** 1496–1503
627 (2020).
628 20. Otto, G. P., Razi, M., Morvan, J., Stenner, F. & Tooze, S. A. A novel syntaxin 6-
629 interacting protein, SHIP164, regulates syntaxin 6-dependent sorting from early endosomes.
630 *Traffic* **11,** 688–705 (2010).
631 21. Pérez-Victoria, F. J. & Bonifacino, J. S. Dual roles of the mammalian GARP complex in
632 tethering and SNARE complex assembly at the trans-golgi network. *Molecular and cellular*
633 *biology* **29,** 5251–5263 (2009).
634 22. Schindler, C., Chen, Y., Pu, J., Guo, X. & Bonifacino, J. S. EARP is a multisubunit
635 tethering complex involved in endocytic recycling. *Nature cell biology* **17,** 639–650 (2015).
636 23. Abascal-Palacios, G., Schindler, C., Rojas, A. L., Bonifacino, J. S. & Hierro, A. Structural
637 basis for the interaction of the Golgi-Associated Retrograde Protein Complex with the t-
638 SNARE Syntaxin 6. *Structure* **21,** 1698–1706 (2013).
639 24. Gillingham, A. K., Bertram, J., Begum, F. & Munro, S. In vivo identification of GTPase
640 interactors by mitochondrial relocalization and proximity biotinylation. *eLife* **8,** e45916
641 (2019).
642 25. Jansen, I. E., Ye, H., Heetveld, S., Lechler, M. C., Michels, H., Seinstra, R. I., Lubbe, S. J.,
643 Drouet, V., Lesage, S., Majounie, E., Gibbs, J. R., Nalls, M. A., Ryten, M., Botia, J. A.,
644 Vandrovcova, J., Simon-Sanchez, J., Castillo-Lizardo, M., Rizzu, P., Blauwendraat, C.,
645 Chouhan, A. K., Li, Y., Yogi, P., Amin, N., Duijn, C. M. van, (IPGDC), I. P. D. G. C., Morris, H.
646 R., Brice, A., Singleton, A. B., David, D. C., Nollen, E. A., Jain, S., Shulman, J. M. & Heutink,
647 P. Discovery and functional prioritization of Parkinson's disease candidate genes from large-
648 scale whole exome sequencing. *Genome biology* **18,** 22 (2017).
649 26. Meers, P., Ali, S., Erukulla, R. & Janoff, A. S. Novel inner monolayer fusion assays reveal
650 differential monolayer mixing associated with cation-dependent membrane fusion.
651 *Biochimica et Biophysica Acta (BBA) - Biomembranes* **1467,** 227–243 (2000).
652 27. Park, J.-S., Thorsness, M. K., Policastro, R., McGoldrick, L. L., Hollingsworth, N. M.,
653 Thorsness, P. E. & Neiman, A. M. Yeast Vps13 promotes mitochondrial function and is
654 localized at membrane contact sites. *MBoC* **27,** 2435–2449 (2016).
655 28. Stenmark, H., Aasland, R. & Driscoll, P. C. The phosphatidylinositol 3-phosphate-
656 binding FYVE finger. *FEBS Letters* **513,** 77–84 (2002).
657 29. Zoncu, R., Perera, R. M., Balkin, D. M., Pirruccello, M., Toomre, D. & De Camilli, P. A
658 Phosphoinositide Switch Controls the Maturation and Signaling Properties of APPL
659 Endosomes. *Cell* **136,** 1110–1121 (2009).
660 30. Nakamura, N., Rabouille, C., Watson, R., Nilsson, T., Hui, N., Slusarewicz, P., Kreis, T. E.
661 & Warren, G. Characterization of a cis-Golgi matrix protein, GM130. *Journal of Cell Biology*
662 **131,** 1715–1726 (1995).
663 31. Lefrancois, S., Zeng, J., Hassan, A. J., Canuel, M., Morales, C. R. The lysosomal
664 trafficking of sphingolipid activator proteins (SAPs) is mediated by sortilin. *The EMBO*
665 *Journal* **22,** 6430–6437 (2003).
666 32. Luzio, J. P., Brake, B., Banting, G., Howell, K. E., Braghetta, P. & Stanley, K. K.
667 Identification, sequencing and expression of an integral membrane protein of the trans-Golgi
668 network (TGN38). *Biochem J* **270,** 97–102 (1990).

669 33. Wakana, Y., van Galen, J., Meissner, F., Scarpa, M., Polishchuk, R. S., Mann, M. &
670 Malhotra, V. A new class of carriers that transport selective cargo from the trans Golgi
671 network to the cell surface. *The EMBO Journal* **31,** 3976–3990 (2012).
672 34. Petersen, C. M., Nielsen, M. S., Nykjær, A., Jacobsen, L., Tommerup, N., Rasmussen, H.
673 H., Røigaard, H., Gliemann, J., Madsen, P. & Moestrup, S. K. Molecular Identification of a
674 Novel Candidate Sorting Receptor Purified from Human Brain by Receptor-associated
675 Protein Affinity Chromatography. *J. Biol. Chem.* **272,** 3599–3605 (1997).
676 35. Porat-Shliom, N., Kloog, Y. & Donaldson, J. G. A Unique Platform for H-Ras Signaling
677 Involving Clathrin-independent Endocytosis. *MBoC* **19,** 765–775 (2008).
678 36. Milovanovic, D., Wu, Y., Bian, X. & De Camilli, P. A liquid phase of synapsin and lipid
679 vesicles. *Science* **361,** 604–607 (2018).
680 37. Milovanovic, D. & Camilli, P. D. Synaptic Vesicle Clusters at Synapses: A Distinct Liquid
681 Phase? *Neuron* **93,** 995–1002 (2017).
682 38. Park, D., Wu, Y., Lee, S.-E., Kim, G., Jeong, S., Milovanovic, D., Camilli, P. D. & Chang,
683 S. Cooperative function of synaptophysin and synapsin in the generation of synaptic vesicle-
684 like clusters in non-neuronal cells. *Nature Communications* **12,** 263 (2021).
685 39. Wheeler, R. J. & Hyman, A. A. Controlling compartmentalization by non-membrane-
686 bound organelles. *Philosophical Transactions of the Royal Society B: Biological Sciences*
687 **373,** 20170193 (2018).
688 40. Willems, J., Jong, A. P. H. de, Scheefhals, N., Mertens, E., Catsburg, L. A. E., Poorthuis,
689 R. B., Winter, F. de, Verhaagen, J., Meye, F. J. & MacGillavry, H. D. ORANGE: A
690 CRISPR/Cas9-based genome editing toolbox for epitope tagging of endogenous proteins in
691 neurons. *PLOS Biology* **18,** e3000665 (2020).
692 41. Waguri, S., Dewitte, F., Le Borgne, R., Rouillé, Y., Uchiyama, Y., Dubremetz, J.-F. &
693 Hoflack, B. Visualization of TGN to Endosome Trafficking through Fluorescently Labeled
694 MPR and AP-1 in Living Cells. *MBoC* **14,** 142–155 (2003).
695 42. Lin, S. X., Mallet, W. G., Huang, A. Y. & Maxfield, F. R. Endocytosed Cation-
696 Independent Mannose 6-Phosphate Receptor Traffics via the Endocytic Recycling
697 Compartment en Route to the trans-Golgi Network and a Subpopulation of Late Endosomes.
698 *MBoC* **15,** 721–733 (2003).
699 43. Carter, A. P., Diamant, A. G. & Urnavicius, L. How dynein and dynactin transport cargos:
700 a structural perspective. *Current Opinion in Structural Biology* **37,** 62–70 (2016).
701 44. Rapali, P., Radnai, L., Süveges, D., Harmat, V., Tölgyesi, F., Wahlgren, W. Y., Katona, G.,
702 Nyitray, L. & Pál, G. Directed Evolution Reveals the Binding Motif Preference of the
703 LC8/DYNLL Hub Protein and Predicts Large Numbers of Novel Binders in the Human
704 Proteome. *PLOS ONE* **6,** e18818 (2011).
705 45. Wang, Y., Huynh, W., Skokan, T. D., Lu, W., Weiss, A. & Vale, R. D. CRACR2a is a
706 calcium-activated dynein adaptor protein that regulates endocytic traffic. *Journal of Cell*
707 *Biology* **218,** 1619–1633 (2019).
708 46. Shintani, M., Tada, M., Kobayashi, T., Kajiho, H., Kontani, K. & Katada, T.
709 Characterization of Rab45/RASEF containing EF-hand domain and a coiled-coil motif as a
710 self-associating GTPase. *Biochemical and Biophysical Research Communications* **357,** 661–
711 667 (2007).
712 47. Maeda, S., Otomo, C. & Otomo, T. The autophagic membrane tether ATG2A transfers
713 lipids between membranes. *eLife* **8,** e45777 (2019).
714 48. Guardia, C. M., Tan, X.-F., Lian, T., Rana, M. S., Zhou, W., Christenson, E. T., Lowry, A.
715 J., Faraldo-Gómez, J. D., Bonifacino, J. S., Jiang, J. & Banerjee, A. Structure of Human
716 ATG9A, the Only Transmembrane Protein of the Core Autophagy Machinery. *Cell Reports*
717 **31,** (2020).

718 49. Ghanbarpour, A., Valverde, D. P., Melia, T. J. & Reinisch, K. M. A model for a
719 partnership of lipid transfer proteins and scramblases in membrane expansion and organelle
720 biogenesis. *PNAS* **118,** (2021).
721 50. Matoba, K., Kotani, T., Tsutsumi, A., Tsuji, T., Mori, T., Noshiro, D., Sugita, Y., Nomura,
722 N., Iwata, S., Ohsumi, Y., Fujimoto, T., Nakatogawa, H., Kikkawa, M. & Noda, N. N. Atg9 is a
723 lipid scramblase that mediates autophagosomal membrane expansion. *Nat Struct Mol Biol*
724 **27,** 1185–1193 (2020).
725 51. Reinisch, K. M., Chen, X.-W. & Melia, T. J. "VTT"-Domain Proteins VMP1 and
726 TMEM41B Function in Lipid Homeostasis Globally and Locally as ER Scramblases. *Contact*
727 **4,** 251525642110244 (2021).
728 52. Claude-Taupin, A., Jia, J., Bhujabal, Z., Garfa-Traoré, M., Kumar, S., da Silva, G. P. D.,
729 Javed, R., Gu, Y., Allers, L., Peters, R., Wang, F., da Costa, L. J., Pallikkuth, S., Lidke, K. A.,
730 Mauthe, M., Verlhac, P., Uchiyama, Y., Salemi, M., Phinney, B., Tooze, S. A., Mari, M. C.,
731 Johansen, T., Reggiori, F. & Deretic, V. ATG9A protects the plasma membrane from
732 programmed and incidental permeabilization. *Nat Cell Biol* 1–13 (2021).
733 53. Wandinger-Ness, A. & Zerial, M. Rab Proteins and the Compartmentalization of the
734 Endosomal System. *Cold Spring Harbor Perspectives in Biology* **6,** a022616–a022616
735 (2014).
736 54. Simonsen, A., Gaullier, J. M., D'Arrigo, A. & Stenmark, H. The Rab5 effector EEA1
737 interacts directly with syntaxin-6. *The Journal of biological chemistry* **274,** 28857–28860
738 (1999).
739 55. Bock, J. B., Lin, R. C. & Scheller, R. H. A new syntaxin family member implicated in
740 targeting of intracellular transport vesicles. *The Journal of biological chemistry* **271,** 17961–
741 17965 (1996).
742 56. Ganley, I. G., Espinosa, E. & Pfeffer, S. R. A syntaxin 10-SNARE complex distinguishes
743 two distinct transport routes from endosomes to the trans-Golgi in human cells. *The Journal*
744 *of cell biology* **180,** 159–172 (2008).
745 57. Rapali, P., Szenes, Á., Radnai, L., Bakos, A., Pál, G. & Nyitray, L. DYNLL/LC8: a light
746 chain subunit of the dynein motor complex and beyond. *The FEBS Journal* **278,** 2980–2996
747 (2011).
748 58. Pérez-Victoria, F. J., Mardones, G. A. & Bonifacino, J. S. Requirement of the Human
749 GARP Complex for Mannose 6-phosphate-receptor-dependent Sorting of Cathepsin D to
750 Lysosomes. *Molecular biology of the cell* **19,** 2350–2362 (2008).
751 59. Gershlick, D. C., Ishida, M., Jones, J. R., Bellomo, A., Bonifacino, J. S. & Everman, D. B.
752 A neurodevelopmental disorder caused by mutations in the VPS51 subunit of the GARP and
753 EARP complexes. *Human Molecular Genetics* **28,** 1548–1560 (2019).
754 60. Guillén-Samander, A., Leonzino, M., Hanna, M. G., IV, Tang, N., Shen, H. & De Camilli,
755 P. VPS13D bridges the ER to mitochondria and peroxisomes via Miro. *Journal of Cell Biology*
756 **220,** (2021).
757 61. Murphy, S. E. & Levine, T. P. VAP, a Versatile Access Point for the Endoplasmic
758 Reticulum: Review and analysis of FFAT-like motifs in the VAPome. *Biochimica et*
759 *Biophysica Acta (BBA) - Molecular and Cell Biology of Lipids* **1861,** 952–961 (2016).
760 62. Cabukusta, B., Berlin, I., van Elsland, D. M., Forkink, I., Spits, M., de Jong, A. W. M.,
761 Akkermans, J. J. L. L., Wijdeven, R. H. M., Janssen, G. M. C., van Veelen, P. A. & Neefjes, J.
762 Human VAPome Analysis Reveals MOSPD1 and MOSPD3 as Membrane Contact Site
763 Proteins Interacting with FFAT-Related FFNT Motifs. *Cell Reports* **33,** 108475 (2020).
764 63. Gómez-Sánchez, R., Rose, J., Guimarães, R., Mari, M., Papinski, D., Rieter, E., Geerts,
765 W. J., Hardenberg, R., Kraft, C., Ungermann, C. & Reggiori, F. Atg9 establishes Atg2-
766 dependent contact sites between the endoplasmic reticulum and phagophores. *The Journal of*
767 *cell biology* jcb.201710116 (2018).

768 64. Davies, A. K., Itzhak, D. N., Edgar, J. R., Archuleta, T. L., Hirst, J., Jackson, L. P.,
769 Robinson, M. S. & Borner, G. H. H. AP-4 vesicles contribute to spatial control of autophagy
770 via RUSC-dependent peripheral delivery of ATG9A. *Nature Communications* **9,** 3958 (2018).
771 65. Pérez-Victoria, F. J., Schindler, C., Magadán, J. G., Mardones, G. A., Delevoye, C.,
772 Romao, M., Raposo, G. & Bonifacino, J. S. Ang2/Fat-Free Is a Conserved Subunit of the
773 Golgi-associated Retrograde Protein Complex. *MBoC* **21,** 3386–3395 (2010).
774 66. Fröhlich, F., Petit, C., Kory, N., Christiano, R., Hannibal-Bach, H.-K., Graham, M., Liu,
775 X., Ejsing, C. S., Farese, R. V. & Walther, T. C. The GARP complex is required for cellular
776 sphingolipid homeostasis. *eLife* **4,** (2015).
777 67. Khakurel, A., Kudlyk, T., Bonifacino, J. S. & Lupashin, V. V. The Golgi-associated
778 retrograde protein (GARP) complex plays an essential role in the maintenance of the Golgi
779 glycosylation machinery. *MBoC* mbc.E21-04-0169 (2021).
780 68. Lesage, S., Drouet, V., Majounie, E., Deramecourt, V., Jacoupy, M., Nicolas, A., Cormier-
781 Dequaire, F., Hassoun, S. M., Pujol, C., Ciura, S., Erpapazoglou, Z., Usenko, T., Maurage, C.-
782 A., Sahbatou, M., Liebau, S., Ding, J., Bilgic, B., Emre, M., Erginel-Unaltuna, N., Guven, G.,
783 Tison, F., Tranchant, C., Vidailhet, M., Corvol, J.-C., Krack, P., Leutenegger, A.-L., Nalls, M.
784 A., Hernandez, D. G., Heutink, P., Gibbs, J. R., Hardy, J., Wood, N. W., Gasser, T., Durr, A.,
785 Deleuze, J.-F., Tazir, M., Destée, A., Lohmann, E., Kabashi, E., Singleton, A., Corti, O., Brice,
786 A., (PDG), F. P. D. G. S. & (IPDGC), I. P. D. G. C. Loss of VPS13C Function in Autosomal-
787 Recessive Parkinsonism Causes Mitochondrial Dysfunction and Increases PINK1/Parkin-
788 Dependent Mitophagy. *American journal of human genetics* **98,** 500–513 (2016).
789 69. Schauder, C. M., Wu, X., Saheki, Y., Narayanaswamy, P., Torta, F., Wenk, M. R., Camilli,
790 P. D. & Reinisch, K. M. Structure of a lipid-bound extended synaptotagmin indicates a role in
791 lipid transfer. *Nature* **510,** 552–555 (2014).
792 70. Bian, X., Saheki, Y. & Camilli, P. D. Ca2+releases E-Syt1 autoinhibition to couple ER-
793 plasma membrane tethering with lipid transport. *The EMBO journal* **37,** 219–234 (2018).
794 71. Zivanov, J., Nakane, T. & Scheres, S. H. W. Estimation of high-order aberrations and
795 anisotropic magnification from cryo-EM data sets in RELION-3.1. *IUCrJ* **7,** 253–267 (2020).
796 72. Zheng, S. Q., Palovcak, E., Armache, J.-P., Verba, K. A., Cheng, Y. & Agard, D. A.
797 MotionCor2: anisotropic correction of beam-induced motion for improved cryo-electron
798 microscopy. *Nat Methods* **14,** 331–332 (2017).
799 73. Rohou, A. & Grigorieff, N. CTFFIND4: Fast and accurate defocus estimation from
800 electron micrographs. *Journal of Structural Biology* **192,** 216–221 (2015).
801
802

803 **FIGURE LEGENDS**
804
805 **Figure 1. In vitro characterization of SHIP164**.
806 **(A)** The fold prediction algorithm Alphafold indicates that SHIP164 harbors an extended ß-sheet
807 folded to resemble a taco-shell, as in VPS13[8]. From left to right: (a) Ribbons representation for
808 the taco-shell "core", predicted with high confidence (b) the extended ß-sheet is shown in two
809 orientations as surface representation, with carbons shown white, oxygens red, nitrogens blue,
810 and sulfurs yellow. The concave surface of the taco-shell is predicted to be entirely hydrophobic,
811 providing a binding site for lipid fatty acid moieties. (c) additional secondary structure that may
812 associate with the "core" is shown; segments discussed in text are indicated.
813 **(B)** SHIP164 co-purifies with phospholipids according to their abundance in cells as assessed by
814 shotgun lipidomics.
815 **(C)** SHIP164 co-migrates with NBD-PE in a native gel. Comparison of NBD-fluorescence that co-
816 migrates with SHIP164 versus with the well-characterized lipid transport module from E-Syt2
817 suggests that each SHIP164 molecule accomodates multiple (~8) phospholipids.
818 **(D)** Schematic drawing explaining the FRET-based lipid transfer and the dithionite-based control
819 for the absence of liposome fusion.
820 **(E)** Assay consistent with transfer of fluorescent lipids from donor to acceptor liposomes by
821 SHIP164 but not by a tether construct lacking a lipid transfer module. An increase in fluorescence
822 observed with donor liposomes only (red arrow) is due to lipid extraction by SHIP164. A larger
823 increase is observed when lipids are subsequently transferred to the acceptor liposomes.
824 **(F)** Dithionite addition excludes that SHIP164 facilitates membrane fusion.
825 **(G)** 2D class averages from negatively stained SHIP164 and MBP-SHIP164, showing tail-to-tail
826 dimerization. MBPs (arrows) are at the ends of the elongated dimer.
827 **(H**) 2D class averages for the cryo-EM reconstruction show a channel running along the length
828 of SHIP164.
829 **(I)** Cryo-EM map of SHIP164 at a resolution of ~8.3 Å, showing a long central cavity with or
830 without the Alphafold model (see panel A-a) superimposed onto it. The docking is approximate
831 because the resolution of the reconstruction is low and because a high confidence model for
832 SHIP164, beyond the ß -sheet taco shell core, is not available.
833 Experiments in panels E-F were performed in triplicate; SD's are indicated.
834
835 **Figure 2. Localization of exogenous SHIP164 points to a role on endocytic**
836 **organelles.**
837 **(A)** Live fluorescence (inverted grays) image of a COS-7 cell expressing exogenous
838 SHIP164^mScarlet-I. Scale bar, 20nm. High magnification of the indicated regions is shown at
839 right. Scale bars, 5µm.
840 **(B)** Live fluorescence (inverted grays) image of a COS-7 cell expressing exogenous 3xFlag-
841 SHIP164^mScarlet-I. Scale bar, 20µm.
842 **(C)** Live image of the cytoplasm of a COS-7 cell expressing exogenous SHIP164^mScarlet-I
843 (magenta) and the endosomal marker GFP-2xHrs^{FYVE} (green). Arrows indicate SHIP164
844 accumulation juxtaposed to endosomal membrane. Scale bar, 5µm.
845 **(D)** High magnification live fluorescence images of COS-7 cell expressing exogenous
846 SHIP164^mScarlet-I (magenta) and the organelle marker indicated at the top (green). The
847 individual channels are shown as inverted grays. Scar bar, 2µm.
848 **(E)** Live image of the cytoplasm of a COS-7 cell expressing exogenous SHIP164-Halo, the
849 endosome marker EEA1-RFP, and the ER marker GFP-Sec61. Scale bar, 2µm. The individual
850 channels are shown as inverted grays. Scar bar, 1µm.
851 **(F)** Time-series of live fluorescence images of exogenous SHIP164-mRFP (magenta) and EEA1-
852 GFP (green). Arrowheads point to a SHIP164 accumulation as it undergoes fission between two
853 EEA1 positive organelles. Time, seconds. Scale bar, 1µm.

854 **(G)** Fluorescence images of a COS-7 cell expressing exogenous SHIP164^mScarlet-I (magenta)
855 and immunolabeled with antibodies against MPR (green) and GM130 (red). Scale bar, 20µm. The
856 individual channels are shown as inverted grays in the higher magnification of the Golgi complex
857 region shown at right. Arrowheads indicate colocalization of exogenous SHIP164 and endogenous
858 MPR. Scale bar, 5µm.
859 **(H-I)** Fluorescence images of RPE-1 cells demonstrating normal Golgi complex localization of
860 MPR in a cell expressing RFP alone (H) and its abnormal localization in a cell expressing both
861 RFP and SHIP164 (H). Cells were immunolabeled with antibodies against MPR (green) and
862 GM130 (magenta). Both the merge image and the single channels are shown. Arrowheads indicate
863 ectopic accumulations of MPR in cells over-expressing SHIP164. Scale bar, 5µm.
864
865 **Figure 3. Correlative light electron microscopy (CLEM) reveals that foci of**
866 **exogenous SHIP164 reflect large accumulations of small vesicles.**
867 **(A)** SHIP164^mScarlet-positive structures juxtaposed to large GFP-WDFY2-positive endosome
868 compartments in a COS-7 cell also expressing untagged Ras^{G12V} to induce micropinosomes. The
869 two EM images (scale bar, 200nm) correspond to the regions framed by two rectangles in the
870 merge fluorescence image (scale bar, 1µm). SHIP164 fluorescence reflects clusters of small
871 vesicles separated from the endosomes by a band occupied by a dense matrix (arrows).
872 **(B and C)** High power view of endosomes of COS-7 cells expressing exogenous
873 SHIP164^mScarlet-I (magenta), GFP-WDFY2 (green), and untagged Ras^{G12V}. Merge fluorescence
874 images are shown at left and FIB-SEM based reconstructions are shown at right. Scale bar, 1µm.
875
876 **Figure 4. Localization of Endogenous SHIP164 on small clusters of vesicular**
877 **structures.**
878 **(A)** Cartoon of wild-type (top) and edited SHIP164^mNG (bottom).
879 **(B)** Western blot of control and edited cell clones for SHIP164, mNG, and GAPDH as a loading
880 control. The different motility of SHIP164 in control and edited clone indicates the incorporation
881 of mNG in the edited SHIP164.
882 **(C)** Cartoon of endogenously edited locus of SHIP164^mNG in HeLa cell. Red, DNA scar as a
883 result of HITI; blue, small Gly-Ser linkers; green, mNG sequence (shortened for brevity by
884 forward slashes).
885 **(D)** Fluorescence image of endogenous SHIP164^mNG (inverted greys) in an edited HeLa knock-
886 in cell. Arrowheads indicate concentration of endogenous SHIP164 at the cell edge, shown at a
887 higher magnification in the inset. Scale bar, 10µm (main field) and 2µm(inset).
888 **(E)** Single channel (inverted grays) fluorescence images of endogenous SHIP164^mNG and
889 endogenous MPR-mScarlet-I in a HeLa double-knock-in cell demonstrating partial colocalization
890 of the two proteins at the cell edge and the selective concentration of MPR in perinuclear area.
891 Scale bar, 10µm. High magnification of the boxed regions is shown at right where arrowheads
892 indicate overlapping fluorescence. Scale bar, 2µm.
893 **(F)** Left to right: Fixed fluorescence image of endogenously tagged SHIP164^mNG (magenta)
894 HeLa cell also expressing mito-BFP (green) for alignment in CLEM analysis. Scale bar, 5µm.
895 Single plane of area outlined in yellow. Fluorescence overlay with FIB-SEM image: numbered
896 boxes mark region of interest of eSHIP164^mNG fluorescence to be aligned with EM image. Scale
897 bar of magnification area, 1µm. Magnification of cluster of vesicles aligned with eSHIP164^mNG
898 fluorescence marked by numbered boxes. Scale bar of EM area, 100nm.
899 **(G)** Reconstruction of cluster 1 from panel F above. SHIP164 associated endosome structures,
900 magenta; ER tubules, yellow.
901 **(H)** Fluorescence image of endogenously tagged SHIP164^mNG in a HeLa knock-in cell also
902 expressing the ER marker RFP-Sec61 (green) demonstrating some SHIP164 foci are in proximity
903 of ER tubules. Scale bar, 1µm.
904

905 **Figure 5. Interaction of SHIP164 with proteins implicated in retrograde traffic to**
906 **the Golgi complex.**
907 **(A)** Live fluorescence image of a COS-7 cell demonstrating partial colocalization of exogenous
908 SHIP164^mScarlet-I (magenta) and mNeonGreen-Stx6 (green) in the Golgi complex area. Scale
909 bar, 10µm. High magnification of the indicated regions is shown at right and the individual
910 channels are shown as inverted grays. Arrowheads indicate overlapping fluorescence. Scale bar,
911 2µm.
912 **(B)** Mass spectrometry-based identification of material affinity-purified onto immobilized
913 SHIP164 or onto a control protein from mouse brain extract. The selective enrichment of
914 DYNLL1/2 peptides on the SHIP164 bait is shown.
915 **(C)** A mixture of MBP-SHIP164$_{1312-1464}$ and DYNLL1/2 was subjected to size exclusion
916 chromatography. Coomassie blue staining of SDS-PAGE of the eluted fractions reveals co-
917 migration of the two proteins.
918 **(D)** Live fluorescence images (inverted grays) of COS-7 cells expressing either GFP-Rab45 (left)
919 or SHIP164^mScarlet-I (right), or both proteins together (only SHIP164 is shown) as indicated.
920 Scale bar, 10µm. Note the massive recruitment of SHIP164 to the centrosomal region in the
921 presence of Rab45. High magnification of the indicated regions is shown at right and the
922 individual channels are shown as inverted grays. Scale bar, 2µm.
923 **(E)** Cartoon of wild-type SHIP164 highlighting (blue) newly identified Stx6 (L_{759}xxYY_{763}) and
924 DYNLL1/2 (V_{1395}TQATQT_{1401}) interaction motifs (see also Fig. 1Aa).
925
926 **Figure 6. Defects in retrograde membrane traffic to the TGN in SHIP164 knockout**
927 **cells.**
928 **(A)** Western blot of control and edited RPE1 cell clones for SHIP164 and for GAPDH as a loading
929 control.
930 **(B)** Left: fluorescence images of a parental control (left) and SHIP164 KO cells (right)
931 immunolabeled with antibodies against EEA1 (green) and GM130 (magenta). Scale bar, 20µm.
932 Right: Quantification of large EEA1 endosomes (>1µm^2) per cell in control and SHIP164 KO cell
933 clones. Middle line, median; +, mean; bars, 10-90 percentiles. Data represents three biological
934 replicates. **, $p<0.01$.
935 **(C)** Live fluorescence (inverted grays) image of parental control (top) and SHIP164 KO (bottom)
936 cells expressing the endosomal marker GFP-2xHrs^{FYVE}. Scale bar, 20µm.
937 **(D)** Left: fluorescence images of parental control (left) and SHIP164 KO cells (right)
938 immunolabeled with antibodies against MPR (green) and GM130 (magenta). Scale bar, 5µm.
939 Right: Quantification of scattered cytoplasmic spots-to-Golgi complex ratio of MPR signal per cell
940 in control and SHIP164 KO cell clones. Middle line, mean; bars, SD. **, $p<0.01$.
941 **(E)** Left: fluorescence images of parental control (left) and SHIP164 KO cells (right)
942 immunolabeled with antibodies against TGN46 (green) and GM130 (magenta). Scale bar, 5µm.
943 Right: Quantification of scattered cytoplasmic spots-to-Golgi complex ratio of TGN46 signal per
944 cell in control and SHIP164 KO cell clones. Middle line, mean; bars, SD. **, $p<0.01$.
945 **(F)** Left: fluorescence images of parental control (left) and SHIP164 KO cells (right)
946 immunolabeled with antibodies against CHC (green) and GM130 (magenta). Scale bar, 5µm.
947 Right: Quantification of scattered cytoplasmic spots-to-Golgi complex ratio of CHC signal per cell
948 in control and SHIP164 KO cell clones. Middle line, mean; bars, SD. **, $p<0.01$.
949 **(G)** Left: fluorescence images of SHIP164 KO cells expressing RFP alone (left) or both RFP and
950 SHIP164 (right) immunolabeled with antibodies against TGN46 (green) and GM130 (magenta).
951 Scale bar, 5µm. Right: Quantification of scattered cytoplasmic spots-to-Golgi complex ratio of
952 TGN46 signal per cell in SHIP164 KO cell clones expressing RFP alone (solid circles) or both RFP
953 and SHIP164 (open circles). Middle line, mean; bars, SD. **, $p<0.01$; *, $p<0.5$.
954 Data of panels D-F reflect three biological replicates and of panel G two biological replicates.
955

956 **Figure 7. Selective properties of SHIP164 vesicle clusters.**
957 **(A)** Live fluorescence (inverted grays) image of a COS-7 cell expressing exogenous ATG9A-GFP.
958 Scale bar, 10nm.
959 **(B)** Live fluorescence (inverted greys) image of a COS-7 cell demonstrating the clustering of
960 exogenous ATG9A-GFP (left) fluorescence in the Golgi complex area from SHIP164^mScarlet-I
961 expression (right). Scale bar, 10µm. High magnification of the indicated regions is shown at right
962 and the individual channels are shown as inverted grays. Arrowheads indicate overlapping
963 fluorescence. Scale bar, 1µm.
964 **(C)** Impact of the expresion of SHIP164 on the localization of ATG9A in cells also overexpressing
965 Rab45. Cells were transfected with both Rab45 and ATG9A without (left) and with (right) the
966 additional expression of SHIP164. Note that in the presence of SHIP164, Rab45 and ATG9A
967 colocalize in a perinuclear spot. Left, live fluorescence image of a COS-7 cell demonstrating no
968 change to the localization of exogenous ATG9A-GFP (green) upon expression of RFP-Rab45
969 (magenta) and Right, fluorescence image of a COS-7 cell demonstrating colocalization of
970 exogenous ATG9A-GFP and RFP-Rab45 upon the expression of SHIP164-Halo (not shown) in the
971 centrosomal region. Scale bar, 10µm. High magnification of the indicated regions is shown at right
972 and the individual channels are shown as inverted grays. Arrowheads indicate overlapping
973 fluorescence. Scale bar, 2µm.
974 **(D)** Live fluorescence (inverted grays) image of a COS-7 cell expressing exogenous UHRF1BP1-
975 Halo. Scale bar, 20nm. High magnification of the indicated regions is shown at right. Scale bar,
976 5µm.
977 **(E)** Live fluorescence image of a COS-7 cell demonstrating partial colocalization of exogenous
978 ATG9A-GFP (green) and UHRF1BP1-Halo (magenta) fluorescence. Scale bar, 10µm. High
979 magnification of the indicated regions is shown at right and the individual channels are shown as
980 inverted grays. Scale bar, 2µm.
981
982 **Supplemental Figure 1.**
983 In vitro characterization of SHIP164. **(A)**(a) Following batch purification using anti-FLAG M2
984 resin, 3XFLAG-SHIP164$_{\Delta 901\text{-}1099}$ was further purified by size exclusion chromatography on a
985 Superdex-200 column. The gel filtration profile is shown (black), along with that for molecular
986 weight standards (light blue). (b) Sample purity was examined by SDS-PAGE. (c) Representative
987 negative stain electron micrograph of 3XFLAG-SHIP164$_{\Delta 901\text{-}1099}$ (50 nM) using FEI Tecnai 12
988 microscope at 120 kV at a nominal magnification of 52,000×. Staining was with 2% uranyl acetate
989 on carbon-coated copper grids that were glow-discharged for 30 s at 22 mA. Green circles
990 represent particles manually picked with a 300 Å mask diameter in RELION-3.1.
991 **(B)** Cryo-EM workflow. Micrographs, including the representative one shown, were collected
992 using Titan Krios G2 transmission electron microscope (Thermo Fisher Scientific) at 300 kV
993 equipped with a K3 summit direct detection camera (Gatan). Green circles represent particles
994 manually picked for initial reference-free 2D classification prior to autopicking.
995 **(C)** The processing workflow yielded a reconstruction with an estimated resolution of 8.3 Å
996 according to the Fourier shell correlation (FSC) = 0.143 criterion.
997
998 **Supplemental Figure 2.**
999 **(A)** Live fluorescence images of a HeLa cell expressing exogenous GFP-SHIP164 (green) and
1000 soluble RFP-Stx6 1-234 (top) or full-length RFP-Stx6 (bottom; magenta). Individual channels are
1001 shown in inverted grays on the left. Scale bar, 10µm.
1002 **(B)** High power views of micropinosomes of a COS-7 cell expressing exogenous
1003 SHIP164^mScarlet-I (magenta) and the early endosomal marker GFP-WDFY2 (green). Untagged
1004 Ras^{G12V} was also expressed to induce macropinosome formation. The individual channels are
1005 shown as inverted grays. Scar bar, 1µm.

1006 **(C)** Live fluorescence image of a COS-7 cell expressing SHIP164-Halo (magenta) and the
1007 dominant negative GFP-Rab5 S34N mutant. Scale bar, 20µm.
1008 **(D)** Fluorescence images of wild-type HeLa cells immunolabeled with antibodies against MPR
1009 (green) and GM130 (red) and without (top) or with transfection of exogenous SHIP164^mScarlet-
1010 I (magenta; bottom) demonstrating abnormal localization of MPR in the cell expressing SHIP164.
1011 The individual channels are shown as inverted grays. Arrowheads indicate colocalization of
1012 exogenous SHIP164 and endogenous MPR. Scale bar, 5µm.
1013 **(E and F)** Fluorescence images of RPE-1 cells demonstrating normal Golgi complex localization
1014 of sortilin in a cell expressing RFP alone (E) and its abnormal localization in a cell expressing both
1015 RFP and SHIP164 (F). Cells were immunolabeled with antibodies against sortilin (green) and
1016 GM130 (magenta). Both the merge image and the single channels are shown. Arrowheads indicate
1017 ectopic accumulations of sortilin in cells over-expressing SHIP164. Scale bar, 5µm.
1018 **(G and H)** Fluorescence images of RPE-1 cells demonstrating normal Golgi complex localization
1019 of TGN46 in a cell expressing RFP alone (G) and its unaffected localization in a cell expressing
1020 both RFP and SHIP164 (H). Cells were immunolabeled with antibodies against TGN46 (green)
1021 and GM130 (magenta). Both the merge image and the single channels are shown. Scale bar, 5µm.
1022
1023 **Supplemental Figure 3.**
1024 High magnification live fluorescence images of COS-7 cell expressing exogenous SHIP164 1-873-
1025 mRFP (magenta) and either the endosome marker WDFY2 or the ER protein Sec61b (green). The
1026 individual channels are shown as inverted grays. Scar bar, 2µm.
1027
1028 **Supplemental Figure 4.**
1029 **(A)** Merge fluorescence image of endogenous SHIP164^mNG (green) and exogenous
1030 SHIP164^mScarlet-I (magenta) in an edited HeLa knock-in cell to demonstrate overlap of the two
1031 fluorescence signals. Scale bar, 10µm. High magnification of the indicated region is shown at right
1032 where the individual channels are shown as inverted grays. Scale bar, 2µm.
1033 **(B)** Merge fluorescence image of endogenous MPR-mScarlet-I and endogenous SHIP164^mNG
1034 in a HeLa double-knock-in cell demonstrating partial colocalization of the two fusion proteins at
1035 the cell edge but not with pulsed EGF-647 (blue) foci. Scale bar, 10µm. High magnification of the
1036 indicated region is shown at right and the individual channels are shown as inverted grays. Open
1037 arrowheads indicate overlapping fluorescence and blue arrowheads an EGF-647-positive
1038 endocytic structure. Scale bar, 2µm.
1039 **(C)** Live fluorescence image of a COS-7 cell expressing FAM174a-mRFP (inverted grays) and
1040 GFP-WDFY2 (not shown). Scale bar, 20µm. High magnification of the indicated regions is shown
1041 at right and the individual channels are shown as inverted grays. Arrowheads indicate overlapping
1042 fluorescence. Scale bar, 2µm.
1043 **(D)** Live fluorescence image of a COS-7 cell demonstrating partial colocalization of exogenous
1044 SHIP164-GFP (green) FAM174a-mRFP (magenta) fluorescence in the cytoplasm. Scale bar,
1045 10µm. High magnification of the indicated regions is shown at right and the individual channels
1046 are shown as inverted grays. Arrowheads indicate overlapping fluorescence. Scale bar, 2µm.
1047
1048 **Supplemental Figure 5.**
1049 **(A)** Live fluorescence images of a HeLa cell expressing exogenous GFP-SHIP164 Y772A, Y773A
1050 (magenta) and RFP-Stx6 (green) showing loss of Stx6 binding by this SHIP164 mutant. Individual
1051 channels are shown in inverted grays on the left. Scale bar, 10µm.
1052 **(B)** High magnification live fluorescence images COS-7 cell expressing exogenous SHIP164
1053 Y772A, Y773A-mRFP and endosome marker EEA1 or the ER marker Sec61b showing that this
1054 SHIP164 mutant still accumulates at hot spots. The individual channels are shown as inverted
1055 grays. Scar bar, 2µm.

1056 **(C)** Live fluorescence images (inverted grays) of wild-type HeLa cell expressing RFP-Rab45, r
1057 endogenous SHIP164^mNG in a HeLa knock-in cell, or HeLa knock-in cell expressing RFP-
1058 Rab45, as indicated. Scale bar, 10µm. Note the massive recruitment of endogenous SHIP164 to
1059 the centrosomal region in the presence of Rab45. High magnification of the indicated regions is
1060 shown at right and the individual channels are shown as inverted grays. Scale bar, 2µm.
1061 **(D)** Impact of the expresion of exogenous SHIP164 on the localization of endogenous MPR-mNG
1062 in cells also overexpressing Rab45. HeLa eMPR-mNG knock-in cells were transfected with Rab45
1063 without (left) and with (right) the additional expression of SHIP164. Note that in the presence of
1064 SHIP164, Rab45 and MPR colocalize in a perinuclear spot. Left, live fluorescence image of a HeLa
1065 knock-in cell demonstrating no change to the localization of endogenous MPR-mNG (green) upon
1066 expression of RFP-Rab45 (magenta) and Right, fluorescence image of a HeLa knock-in cell
1067 demonstrating colocalization of endogenous MPR-mNG and RFP-Rab45 upon the expression of
1068 SHIP164-Halo (not shown) in the centrosomal region. Scale bar, 10µm. High magnification of the
1069 indicated regions is shown at right and the individual channels are shown as inverted grays.
1070 Arrowheads indicate overlapping fluorescence. Scale bar, 2µm.
1071 **(E)** Live fluorescence image of a COS-7 cell expressing SHIP164^mScarlet-I (magenta) and the
1072 dominant negative GFP-Rab45 S555N mutant (green) showing that this Rab45 mutant does not
1073 recruit SHIP164. Individual channel shown in inverted gray. Scale bar, 20µm.
1074
1075 **Supplemental Figure 6.**
1076 **(A)** Sequencing results confirming editing of SHIP164 locus in RPE1 cells. PAM sequence (green)
1077 was directed to exon 2 and each clone was found to have a mutation starting four nucleotides
1078 upstream. # Indicates nucleotide is the same between parental control and clone 2.
1079 **(B)** Left: Fluorescence images of a parental control (left) and SHIP164 KO cells (right)
1080 immunolabeled with antibodies against sortilin (green) and GM130 (magenta). Scale bar, 5µm.
1081 Right: Quantification of the scattered cytoplasmic spots-to-Golgi complex ratio of Sortilin signal
1082 per cell (circles) in control and SHIP164 KO cell clones. Middle line, mean; bars, SD. Data
1083 represents three biological replicates. **, $p<0.01$.
1084 **(C)** Fluorescence images of a SHIP164 KO cell immunolabeled with antibodies against TGN46
1085 (green) and MPR (magenta) demonstrating distinct post-Golgi vesicle populations. Scale bar,
1086 5µm. High magnifications of the indicated regions are shown as insets and the individual channels
1087 are shown as inverted grays. Arrowheads indicate divergent fluorescence. Scale, 2µm.
1088 **(D)** Fluorescence images of a SHIP164 KO cells expressing both RFP and SHIP164 (not shown)
1089 immunolabeled with antibodies against the indicated proteins (green) and GM130 (magenta).
1090 Scale bar, 5µm.
1091 **(E)** Fluorescence images of parental control or SHIP164 KO cells expressing either RFP alone
1092 (not shown) or RFP and exogenous untagged SHIP164 (not shown) immunolabeled with
1093 antibodies against the EEA1 (green) demonstrating that overexpression of SHIP164, even in KO
1094 cells, reuslts in EEA1 accumulations not typically found in wild-type cells where SHIP164 is not
1095 over-expressed (far left). Scale bar, 10µm.
1096 **(F)** Western blot of RPE1 cells for SHIP164 and for GAPDH as a loading control, either treated
1097 with control or SHIP164 specific siRNAs.
1098 **(G)** Left: Fluorescence images of a wild-type cells treated with control (left) or SHIP164 specific
1099 siRNAs (right) immunolabeled with antibodies against EEA1 (green). Scale bar, 20µm. Right,
1100 Quantification of large EEA1 endosomes (>1µm^2) per cell in control and SHIP164 knock-down
1101 cell. Middle line, median; +, mean; bars, 10-90 percentiles. Data represents three biological
1102 replicates. **, $p<0.01$.
1103
1104 **Supplemental Figure 7.**

1105 High magnification live fluorescence image COS-7 cell expressing exogenous UHRF1BP1-Halo
1106 (magenta) and the lysosomal marker LAMP1-GFP (green). The individual channels are shown as
1107 inverted grays. Scar bar, 2μm.
1108
1109 **Supplemental movie 1**
1110 High magnification of live fluorescence time series of COS-7 cell expressing exogenous SHIP164-
1111 mRFP (magenta) and the endosomal marker EEA1-GFP (green) demonstrating the dynamics of
1112 SHIP164 accumulations. Frames captured every 2s. Scale bar, 1μm.
1113
1114 **Supplemental movie 2**
1115 Zoom of live fluorescence time series of a double-knock-in HeLa cell demonstrating the
1116 colocalization of fluorescencnt signal from endogenous MPR-mScarlet-I (magenta; left) and
1117 endogenous SHIP164^mNG (green; right) puncta at the cell periphery. Arrowheads indicate
1118 puncta positive for both mScarlet-I and mNG fluorescence. Frames captured every 2s. Scale bar,
1119 10μm.
1120

1121 **MATERIALS AND METHODS**
1122
1123 **Antibodies and Reagents**
1124 The list of antibodies, their working dilution, and the supplier for this study can be found in **Table**
1125 **S1**. All Halo-tag ligands used (JF549 and JF646) were a kind gift from Luke Lavis (Janelia
1126 Research Campus). All SHIP164 (UHRF1BP1L) ORFs used in this study utilized a human codon
1127 optimized sequence designed and purchased from Genscript (sequence available upon request).
1128 The following constructs were kind gifts: BFP-Rab5b and mito-BFP from G. Voeltz (University of
1129 Colorado-Boulder, CO; Addgene plasmids #49147, #49151, respectively); Sec61b-GFP and RFP
1130 from T. Rapoport (Harvard University, Cambridge, MA); GFP-2xHrs^{FYVE} from Harald Stenmark
1131 (University of Oslo, Norway; Addgene plasmids #140047). Other plasmids encoding EEA1,
1132 WDFY2, APPL1, 2xFYVE were previously generated in the De Camilli lab. All other ORFs used
1133 are listed in **Table S2**.
1134
1135 All EM reagents were purchased from Electron Microscopy Sciences (Hatfield, PA).
1136
1137 Lipids were purchased from Avanti Polar Lipids: DOPC (850357), liver PE (840026), DGS-NTA
1138 (Ni; 790404), brain PI(4,5)P2 (840046), Rh-PE (810150), and NBD-PE (810145).
1139
1140 **Generation of Plasmids**
1141 Codon optimized human SHIP164 generated by Genscript was amplified using PCR from the
1142 pUC57 plasmid and ligated into various mammalian and bacterial expression plasmids. Most
1143 constructs were generated with regular cloning protocols or through site-directed mutagenesis.
1144 The desired ORFs were amplified by PCR and inserted into plasmids through enzyme digestions
1145 and ligation. Some amplified ORFs were ligated using HiFi assembly (NEB). Details of primer
1146 sets, enzymes, techniques, and plasmids used for each construct can be found in **Table S2**.
1147
1148 For internal tagging of SHIP164, the codon optimized human sequence was first amplified by PCR
1149 and cloned into p3xFLAG between the EcoRI/KpnI restriction sites using HiFi assembly. From
1150 there, the ORF of mScarlet-I was amplified by PCR and ligated into the EcoRV site at residue 915
1151 of SHIP164 using HiFi assembly. To generate the amino-terminal free version,
1152 SHIP164^mScarlet-I was amplified by PCR and ligated into pcDNA3.1 His-A between the
1153 HindIII/XhoI sites removing the His_6 tag. Unless stated otherwise, all mutations in this study
1154 were generated using site directed mutagenesis. All ORFs were sequenced in their entirety after
1155 cloning and before use in any and all experiments.
1156
1157 For the MBP-SHIP164 fusion construct used in the in vitro analysis, sequences coding for residues
1158 27–392 of E. coli maltose binding protein (MBP) and two additional alanines were fused to the
1159 N-terminus of SHIP164$_{\Delta 901–1099}$ using Gibson Assembly and site-directed mutatgenesis.
1160
1161 The tethered SHIP164 construct used to perform the *in vitro* lipid transfer assay was generated
1162 using Gibson Assembly as previously described[6], and consists of SHIP164$_{\Delta 901–1099}$ followed by the
1163 unstructured region of human Esyt2(residues 649–689), then the pleckstrin homology domain
1164 of rat PLCΔ(residues 11–140), the unstructured region of Eyst2(residues 690–739), and a
1165 hexahistidine tag at the C-terminus.
1166
1167 **Protein Expression and Purification**
1168 For lipid transfer and cryo-EM studies, 3×FLAG-SHIP164$_{\Delta 901-1099}$ constructs were transfected into
1169 Expi293F cells (Thermo Fisher Scientific) according to manufacturer instructions. Protein
1170 expression was enhanced by the addition of nonessential amino acids (Gibco) and valproic acid
1171 (3.5 mM final concentration) 16 h after transfection. Cells were harvested by centrifugation 65 h

after transfection and either flash-frozen for storage or used immediately for protein purification. Cells were lysed by 3 freeze-thaw cycles in buffer (50 mM HEPES pH 8.0, 500 mM NaCl, 1 mM TCEP, 5% glycerol) containing 1× complete EDTA-free protease inhibitor cocktail (Roche). Insoluble debris was removed by centrifugation at 15000 rpm for 30 min, and clarified lysate was mixed with anti-FLAG M2 resin (Sigma) for 3 h while rotating at 4°C. Resin was then washed with 3×10 bed volumes of buffer and subsequently incubated for 18 h at 4°C in buffer supplemented with 1 mM ATP and 2 mM $MgCl_2$. Resin was washed again with 3 bed volumes of buffer and then eluted in 5×0.5 bed volumes of buffer containing 0.25 mg/mL 3×FLAG peptide (APExBio). The protein was further purified by gel filtration (Superdex 200 10/300 GL, GE Healthcare) and concentrated to approximately 1.5 μM (Amicon). E-Syt2 was expressed and purified as previously described[69].

The MBP-SHIP164$_{1312-1464}$/DYNLL1 complex was recombinantly expressed in BL21 DE3 competent cells for purification and size exclusion chromatography analysis using the polycistronic pET Duet expression plasmid, details of which can be found in **Table S2**. BL21 cells transformed with the dual expression plasmid were grown at 37°C in super broth (SB) media (1L) until reaching an OD_{600} between 2 and 3, after which the temperature was turned down to 18°C and cells were induced with 0.25mM IPTG for 16 hours with continuous shaking. Cells were pelleted in a floor centrifuge at 4000g for 15 minutes and then resuspended in lysis buffer (25mM Tris pH 7.5, 200mM NaCl, 0.1% Tween-20) and frozen at -80°C until ready for purification. For purification, the pellet was thawed in a water bath and then sonicated until the desired lysis using a macro sonicator tip (VirTris VirSonic). Membrane and un-sonicated material were pelleted in a floor ultra-centrifuge at 24,000g for 20 minutes and the supernatant was collected and incubated with 250uL of amylose resin for 1 hour rotating at 4°C. The resin was then washed three times with 40x bed volumes of ice-cold wash buffer (25mM Tris pH 7.5, 200mM NaCl, 1mM BME). Two elutions were performed from the resin using 2x bed volume of elution buffer (25mM Tris pH 7.5, 150mM NaCl, 10mM maltose, 1mM BME). The eluate was collected and run over a Superdex S200 column using a GE AKTA pure system, and individual fractions (1mL) were collected for analysis by SDS-PAGE and Coomassie staining.

Lipidomics Analysis of SHIP164 by Mass Spectrometry

Full length human 3xFLAG-SHIP164 was expressed and purified as described above with the following modifications. Following immunoprecipitation, FLAG resin bound SHIP164 was washed with 3x100 bed volumes of sonication buffer containing 1mM BME and protease inhibitor cocktail for 20 minutes. After elution, the protein was buffer exchanged into 50mM mass spectrometry grade ammonium acetate. The purified protein sample and $1x10^7$ untransfected Expi293F cells was sent to Avanti Polar Lipids for analysis. Lipids were extracted in 2:1 (v/v) methanol:chloroform. The chloroform layer was dried, and lipids were reconstituted with internal standards for PC, PE, PI, PS, PA, PG, SM, TAG, DAG, and CE for quantification. As described by the company, the sample was injected into a reverse phase C8 column with a gradient elution profile for the resolution required of each lipid class and detected by an AB Sciex 5500 tandem mass spectrometer. The molecular species of lipids was quantified based on internal standards and summed by lipid class.

Native gel lipid binding assay.

Purified E-Syt2 and SHIP164$_{\Delta 901-1099}$ at indicated concentrations were mixed with methanol-dissolved NBD-PE (0.2 mM final concentration) in 20-μL total reaction volumes and incubated for 2 h on ice. Samples were loaded on 4–20% Mini-PROTEAN TGX Precast Gels and run for 3 h at 200 V. NBD fluorescence was visualized using an ImageQuant LAS4000 (GE Healthcare), and gels were stained with Coomassie Brilliant Blue R (Sigma Aldrich) to visualize total protein. A

1222 standard curve was generated using the fluorescence values of E-Syt2 and the quantity of lipid
1223 bound to SHIP164 was analyzed using ImageJ (National Institutes of Health).
1224
1225
1226 **FRET-based lipid transfer assay.**
1227 Liposomes were prepared as previously described[6]. Briefly, lipids in chloroform were mixed in the
1228 indicated ratios and dried to thin films, then resuspended in buffer containing 50 mM HEPES,
1229 pH 8.0, 500 nM NaCl, 1 mM TCEP, and 5% glycerol to 1 mM total lipid concentration. Rehydrated
1230 lipids were then incubated at 37°C for 1 h before being subjected to 10 freeze-thaw cycles. Crude
1231 liposomes were freshly extruded through a polycarbonate filter with 100-nm pore size prior to
1232 transfer assays.
1233
1234 Lipid transfer experiments were set up in 100-µL reaction volumes containing 0.125 µM protein,
1235 25 µM donor liposomes (61% DOPC, 30% liver PE, 2% NBD-PE, 2% rhodamine-PE, and 5% DGS-
1236 NTA[Ni]) and 25 µM acceptor liposomes (65% DOPC, 30% liver PE, and 5% PI(4,5)P_2. Donor and
1237 acceptor liposomes were included in the reaction for 5 minutes prior to the addition of protein to
1238 establish a fluorescence baseline. The lipid transfer reaction was monitored via NBD fluorescence
1239 intensity detected every 1 min at 538 nm upon excitation at 460nm. Lipid transfer assay was
1240 performed for 1 h at 30°C in a 96-well plate (Nunc) using a Synergy H1 Plate Reader (BioTek).
1241
1242 A tether-only construct consisting of an N-terminal hexahistidine-tagged plexstrin homology
1243 domain from rat PLCΔ(11-140) was expressed and purified as previously described[70]. The lipid
1244 transfer assay using this construct was performed using the same protein:lipid ratio.
1245
1246 A dithionite assay, to rule out the possibility that the NBD fluorescence increase was due to
1247 SHIP164-mediated liposome fusion, was performed in the same way as the transfer assay, except
1248 for the final addition of 5 µL freshly prepared dithionite buffer [100 mM dithionite (Sigma
1249 Aldrich) in 50 mM Tris, pH 10] after fluorescence increase observed during the transfer assay had
1250 reached its maximum. NBD emission was then monitored for an additional 30 min.
1251
1252 **Cryo-EM sample preparation, data collection, and image processing**
1253 Purified SHIP164$_{\Delta 901\text{-}1099}$ was supplemented with 0.05% n-Octyl-β-D-glucoside immediately
1254 before cryo-EM samples were prepared. Quantifoil R1.2/1.3 300 mesh copper grids were glow
1255 discharged for 30 s at 22 mA, then 4 µL of sample was applied. The grids were blotted with a single
1256 blotting paper for 5.5 s at a blot force of -2 in 90% humidity at 4°C before being plunge-frozen in
1257 liquid ethane using an FEI Vitrobot Mark IV (Thermo Fisher Scientific).

1258 Data collection was performed on a Titan Krios G2 transmission electron microscope (Thermo
1259 Fisher Scientific) at 300 kV with a K3 summit direct detection camera (Gatan). SerialEM was used
1260 to collect 5,381 movies at a nominal magnification of 81,000× in super-resolution mode with a
1261 magnified pixel size of 1.068Å on the specimen level (counting mode). Movies were dose-
1262 fractionated into 43 frames of 0.08 seconds each at a dose rate of 16.9 electrons/Å^2 per s for a
1263 total dose of 51 e^-/Å^2. The defocus range for the sample was between 1.4 and 2.4 µm.

1264 Image processing was carried out using RELION-3.1[71]. The 5,381 micrographs were motion-
1265 corrected and dose-weighted in MotionCor2[72] with a binning factor of 2 and divided into 5×5
1266 patches. The contrast transfer function was calculated with CTFFIND-4.1[73]. Reference-free 2D
1267 classification of 1,044 manually picked particles was done, and the three best classes that showed
1268 well-defined particles were used as references for autopicking that yielded a dataset of 3.36
1269 million particles. Multiple rounds of 2D classification were carried out to remove ice
1270 contamination and bad particles. The subset of the most homogeneous 254,169 particles was used

1271 to generate a 3D initial model using stochastic gradient descent with C1 symmetry as implemented
1272 in RELION, and 3D classification further isolated 86,720 particles. This 3D class underwent auto-
1273 refinement and post-processing for a final reconstruction at a resolution of 8.3 Å according to the
1274 Fourier shell correlation (FSC) = 0.143 criterion.

1275 **Correlative Light and Electron Microscopy**
1276 For TEM CLEM, COS-7 cells were plated on 35 mm MatTek dish (P35G-1.5-14-CGRD) and
1277 transfected as described above with SHIP164^mScarlet-I, GFP-WDFY2, mito-BFP, and Ras^{G12V}.
1278 Cells were pre-fixed in 4% PFA in Live Cell Imaging Buffer (see above) then washed before
1279 fluorescence light microscopy imaging. Regions of interest were selected and their coordinates on
1280 the dish were identified using phase contrast. Cells were further fixed with 2.5% glutaraldehyde
1281 in 0.1 M sodium cacodylate buffer, postfixed in 2% OsO_4 and 1.5% $K_4Fe(CN)_6$ (Sigma-Aldrich) in
1282 0.1 M sodium cacodylate buffer, en bloc stained with 2% aqueous uranyl acetate, dehydrated, and
1283 embedded in Embed 812. Cells of interest were relocated based on the pre-recorded coordinates.
1284 Ultrathin sections (50-60 nm) were observed in a Talos L 120C TEM microscope at 80 kV, images
1285 were taken with Velox software and a 4k × 4K Ceta CMOS Camera (Thermo Fisher Scientific). For
1286 FIBSEM CLEM, mito-BFP was expressed in endogenously tagged eSHIP164^mNG HeLa cells
1287 processed as above except the dehydration was implemented at the low temperatures gradually
1288 decreased from 0 °C to -50 °C. Epon blocks were glued onto the SEM sample mounting aluminum
1289 and platinum *en bloc* coating on the sample surface was carried out with the sputter coater (Ted
1290 Pella, Inc., Redding, California). Sample were FIBSEM imaged in a Crossbeam 550 FIBSEM
1291 workstation operating under SmartSEM (Carl Zeiss Microscopy GmbH, Oberkochen, Germany)
1292 and Atlas engine 5 (Fibics incorporated, Ottawa, Canada). The imaging resolution was set at 5
1293 nm/pixel in the X, Y axis with milling being performed at 2.5 nm/step along the Z axis (binned
1294 down by 2 to 5 nm when images were exported) to achieve an isotropic resolution of 5nm voxel.
1295 Images were aligned and exported with Atlas 5 (Fibics incorporated, Ottawa, Canada), further
1296 processed and analyzed with DragonFly Pro software [Object Research Systems (ORS) Inc.,
1297 Montreal, Canada]. Except noted all reagents were from EMS (Electron Microscopy Sciences),
1298 Hatfield, PA.
1299
1300 **Cell culture and Transfections**
1301 hTERT-RPE1 cells were a kind gift of A. Audhya (University of Wisconsin, Madison, WI). HeLa
1302 and COS-7 cells were obtained from ATCC. All mammalian cells were maintained at 37°C in
1303 humidified atmosphere at 5% CO_2 unless noted otherwise. HeLa and COS-7 cells were grown in
1304 DMEM and RPE1 cells in DMEM/F12 medium (Thermo Fisher Scientific) supplemented with
1305 10% FBS, 100 U/mL penicillin, 100mg/mL streptomycin, and 2mM glutamax (Thermo Fisher
1306 Scientific). Expi293F were grown to manufacturers specification in Expi293 expression medium
1307 with constant shaking. All cell lines were routinely tested and always resulted free from
1308 mycoplasma contamination.
1309
1310 Transient transfections were carried out on cells that were seeded at last 8 hours prior. All
1311 transfections of plasmids used FugeneHD (Promega) to manufacturers specifications for 16-24
1312 hours in complete media without antibiotics. Expi293 transfections were carried out to
1313 manufacturers specifications and reagents. siRNAs (IDT) for knowck-down experiments against
1314 SHIP164 (design ID: hs.Ri.UHRF1BP1L.13.2) were transfected using Lipofectamine RNAiMAX
1315 (ThermoFisher) for 48 hours before fixation for immunocytochemistry experiments or collected
1316 for immunoblotting (see below)
1317
1318 **Immunoblotting and Imaging Procedure**
1319 All cell samples analyzed by immunoblotting (RPE1 and HeLa) were scraped from plates and
1320 harvested by centrifugation (500xg for 5 minutes). The pellet was washed with ice-cold PBS and

1321 centrifuged again in a 1.7mL Eppendorf tube. The cells pellet was resuspended in Lysis buffer
1322 (20mM Tris-HCl pH 7.5, 150mM NaCl, 1mM EDTA) containing protease inhibitor cocktail
1323 (Roche) and lysed using mechanical disruption (Isobiotec Cell Homogenizer). The lysate was
1324 clarified by centrifugation (17,000xg for 10 minutes) and then mixed with 3x SDS sample buffer
1325 (Cold Spring Harbor) to 1x concentration and then heated to 95C for 5 minutes. A small portion
1326 of lysate was reserved for quantification of protein concentration by Bradford. 15-25ug of protein
1327 samples were separated by electrophoresis on a 4-20% Mini-PROTEAN TGX gel and then
1328 subjected to standard western blot transfer and procedures. Blots were imaged using the Odyssey
1329 imaging system (Licor) using manufacturers protocols. All primary antibodies used in this study
1330 are listed in **Table S1**.
1331
1332
1333 **Live Cell Imaging and Immunofluorescence**
1334 For all live cell microscopy cells were seeded on glass-bottom mat-tek dishes (MATtek
1335 corporation) 5500/cm² in complete media. Transfections were carried out as described above.
1336 Spinning-disk confocal imaging was preformed 16-24 post transfection using an Andor Dragon
1337 Fly 200 (Oxford Instruments) inverted microscope equipped with a Zyla cMOS 5.5 camera and
1338 controlled by Fusion (Oxford Instruments) software. Laser lines used: DAPI, 440nm; GFP, 488;
1339 RFP, 561; Cy5, 647. Images were acquired with a PlanApo objective (60x 1.45-NA). During
1340 imaging, cells were maintained in Live Cell Imaging buffer (Life Technologies) in a cage incubator
1341 (Okolab) with humidified atmosphere at 37C.
1342
1343 Halo-tag ligands ligands were used at a final concentration of 200nM. Cells were incubated with
1344 indicated dye for 45 minutes in complete media, rinsed three times with complete media, and
1345 then incubated in complete media for 45 minutes before imaging. Immunofluorescent
1346 experiments were performed with cells grown on #1 glass cover slips. Cells were fixed with 4%
1347 PFA in fixation buffer (400mM sucrose, 125mM NaCal, 5mM KCl, 1mM NaH2PO4, 2mM MgCl2,
1348 5mM glucose, 1mM EGTA, 5mM PIPES) for 10 mins at 37°C, washed 3x with TBS (Tris-HCl pH
1349 7.5, 150mM NaCl), permeabilized using 1x PBS containing 0.5% Triton for 10 min at RT and then
1350 blocked using antibody dilution buffer (50 mM Tris pH 7.5, 150 mM NaCl, 0.1% Triton, 4% BSA)
1351 for 1 hour at 25°C. Coverslips were incubated with the indicated primary antibody diluted in the
1352 same buffer overnight at 4°C. Slides were washed with PBS containing 0.1% Triton to remove
1353 excess primary antibody and subsequently incubated with the indicated secondary antibody
1354 diluted in antibody dilution buffer for 45 min at room temperature in the dark prior to mounting.
1355
1356 **Generation of CRISPR edited Cell Lines**
1357 SHIP164 RPE1 knockout cells were generated by first identifying a guide RNA (gRNA) directed to
1358 exon 2 of SHIP164 using a Cas9 target identification tool (CHOPCHOP). A single stranded oligo
1359 (IDT) was synthesized containing the sense sequence and then cloned into PX458 (Addgene
1360 #48138) and transfected into RPE1 cells. 48 hours post transfection cells were single cell sorted
1361 using FACS Aria based on GFP expression into 96-well plates, and individual clones were grown
1362 out and subsequently examined by immunoblot analysis. Sanger sequencing was used to confirm
1363 the presence of mutations, which led to frameshifts and premature stop codons within the coding
1364 sequence of SHIP164. Two validated clones were used in subsequent studies.
1365
1366 Endogenous tagging of in HeLa cells was carried out using the ORANGE system. Briefly, a gRNA
1367 targeted close the desired site within the endogenous reading frame of the indicated target protein
1368 was identified and subsequently cloned into empty pORANGE using HiFi assembly at the tandem
1369 BbsI site. The ORF of the indicated fluorescent protein (mNeonGreen or mScarlet-I) with linker
1370 regions to make an in-frame insertion was cloned into the HindIII/XhoI sites of pORANE using
1371 standard restriction enzyme cloning. The finalized plasmid was transfected into wild-type HeLa

1372 cells using the transfection protocol described above. Cells were split once to keep confluency
1373 below 80% and 5-days post transfection and the cells were imaged using confocal microscopy.
1374 After visualizing cells positive for the correct fluorescent protein, cells were serially diluted and
1375 plated at 10 cells per well on a glass bottom 96-well plate (Cellvis P96-1-N) and inspected for
1376 fluorescence when the wells were sub-confluent. Wells with positive fluorescence were expanded,
1377 serially diluted, and plated at one cell per wll on a glass bottom 96-well plate and inspected for
1378 fluorescence when the clones were sub-confluent. All gRNAs used in this study are listed in **Table**
1379 **S2.**
1380
1381 **Mouse Brain Lysate Preparation, Affinity Purification, and Protein Identification**
1382 Brains were collected from sacrificed wild-type C57/black mice. For each 1g of whole brian
1383 material, 10 mL of buffer (25mM HEPES pH 7.4, 200mM NaCl, 5% glycerol, protease inhibitors)
1384 was added. Mechanical lysis was performed using a glass dounce-homogenizer (15 strokes).
1385 Triton X-100 was added to 1% and material was rotated at 4C for 30 minutes. Material was
1386 centrifuged at 1000g to remove cell debris and the collected supernatant was centrifuged at
1387 27000g for 20 minutes. The resulting supernatant was flash frozen and stored at -80C until use.
1388
1389 Purified 3xFLAG-SHIP164 or FLAG-tagged control protein was immobilized on anti-FLAG resin
1390 as described above. Immobilized SHIP164 and control protein was incubated with mouse brain
1391 lysate for 16hrs gently rotating at 4C. Resin was spun down and the supernatant was removed
1392 before 2x10 bed volume washes using a wash buffer (25mM HEPES pH 7.4, 150mM NaCl, 1mM
1393 BME, protease inhibitors). Protein bound to resin was boiled in the same wash buffer and eluate
1394 was transferred to a new Eppendorf tube. Protein in the eluate was precipitated using
1395 trichloroacetic acid (TCA) on ice for 16hrs, neutralized using Tris pH 8.5 buffer, and then the
1396 precipitate was pelleted in a table top centrifuge. The precipitate was washed twice with ice cold
1397 acetone and then dried using a speed-vac. Protein and peptide identification was achieved by
1398 shotgun tandem LC-MS/MS analysis. Analysis was performed using Scaffold 5 proteome software
1399 to identify promising identifications.
1400
1401 **Image processing, Analysis, and Statistics**
1402 Florescence images presented in this study are representative of cells imaged in at least three
1403 independent experiments and were processed with ImageJ software. The dimensions of some of
1404 the magnification insets or panels were enlarged using the *Scale* function on ImageJ.
1405
1406 Quantification of vesicle-to-Golgi ratio and peripheral structures: unprocessed images with two
1407 channels (GM130 for Golgi in one channel and the protein of interest in the other channel) were
1408 made into maximum intensity projections. A mask of the Golgi complex was made using the
1409 GM130 signal and then used to subtract the Golgi signal from the signal of the entire cell protein
1410 of interest channel resulting in peripheral signal only. Outlines of individual cells were drawn,
1411 and the amount of peripheral signal was measured and then divided by the extracted Golgi signal
1412 for each cell to obtain the ratio. Where stated that the number of peripheral structures were
1413 counted, the subtracted peripheral image was made into a mask to identify structures of the
1414 indicated area and subsequently counted per cell.
1415
1416 Statistical analysis was performed with GraphPad Prism 7 software. Groups were compared using
1417 a two-tail unpaired Student *t* test and results were deemed significant when a p value was smaller
1418 than 0.05.
1419

1420 **TABLES**
1421
1422 **Table S1.** List of antibodies used in this study.
1423

Protein (epitope)	Company; Catalog number	Antibody species	Working dilution for immunocytochemistry	Working dilution for immunoblotting
GM130	BD Bioscience; 610822	Mouse	1:100	N/A
GM130	Abcam; ab30637	Rabbit	1:300	N/A
EEA1	BD Bioscience; 610457	Mouse	1:100	N/A
EEA1	Thermo Scientific; PA1-063A	Rabbit	1:400	N/A
Sortilin	Abcam; ab243043	Rabbit	1:500	N/A
MPR (IGF-IIR)	Santa Cruz Biotechnology; sc-53146	Mouse	1:100	N/A
TGN46	Abcam; ab50595	Rabbit	1:200	N/A
TGN46	AbD Serotec; AHP500GT	Sheep	1:300	N/A
mNeonGreen	ChromoTek; 32f6-100	Mouse	1:500	1:1000
SHIP164	Custrom antibody produced by Proteintech	Rabbit	N/A	1:500
GAPDH	Proteus; 40-1246	Mouse	N/A	1:1000

1424
1425 **Table S2.** List of ORFs and primers used for cloning in this study.
1426 *See associated excel file.*
1427

ACKNOWLEDGMENTS

We thank members of the De Camilli and Reinisch lab for critical reading of the manuscript. We also thank Shan Xu and Song Pang (Janelia Research Labs) for help and discussion with FIB-SEM experiments. This work was in supported in part by grants from the NIH (NS36251, DA18343 and DK45735), the Kavli Institute for Neuroscience, and the Parkinson Foundation to PDC, the NIH (R35GM131715) to KMR, the NIH (F32NS108448) to MGH, and the NIH (T32GM008283) to PS. This research was also funded in part by Aligning Science Across Parkinson's grant ASAP-000580 through the Michael J. Fox Foundation for Parkinson's Research (MJFF) to PDC and KMR. For the purpose of open access, the author has applied a CC BY public copyright license to all Author Accepted Manuscripts arising from this submission.

AUTHOR CONTRIBUTIONS

MGH, PS, KMR, PDC conceptualized the project. PS performed structural analysis and lipid binding and transport experiments, YW performed CLEM experiments in collaboration with MGH, and MGH performed everything else. MGH, PS, YW, KMR, PDC analyzed data. MGH, PS, KMR, PDC wrote the original draft of the manuscript, which was then reviewed and edited by all the authors.

CONFLICT OF INTEREST

PDC is a member of the Scientific Advisory Board of Casma Therapeutics. No conflict exists with this role

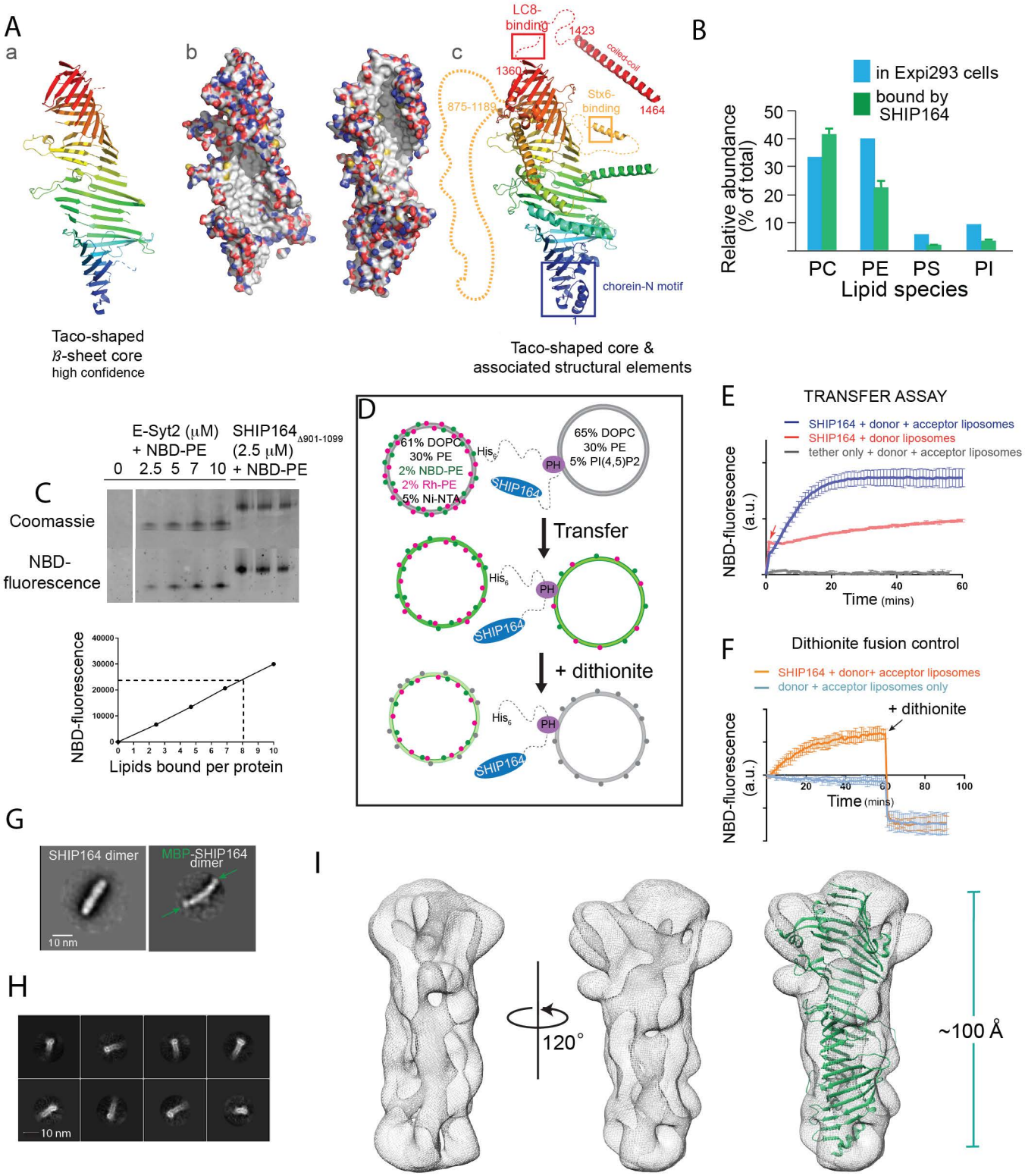
A
a
b
c
LC8-binding
1423
coiled-coil
1360
875-1189
Stx6-binding
1464
chorein-N motif
Taco-shaped
β-sheet core
high confidence
Taco-shaped core &
associated structural elements
B
in Expi293 cells
bound by SHIP164
Relative abundance (% of total)
50
40
30
20
10
PC
PE
PS
PI
Lipid species
C
E-Syt2 (μM) + NBD-PE
SHIP164Δ901-1099 (2.5 μM) + NBD-PE
0 2.5 5 7 10
Coomassie
NBD-fluorescence
NBD-fluorescence
40000
30000
20000
10000
0
0 1 2 3 4 5 6 7 8 9 10
Lipids bound per protein
D
61% DOPC
30% PE
2% NBD-PE
2% Rh-PE
5% Ni-NTA
His6
PH
SHIP164
65% DOPC
30% PE
5% PI(4,5)P2
Transfer
+ dithionite
E
TRANSFER ASSAY
SHIP164 + donor + acceptor liposomes
SHIP164 + donor liposomes
tether only + donor + acceptor liposomes
NBD-fluorescence (a.u.)
0
20
40
60
Time (mins)
F
Dithionite fusion control
SHIP164 + donor+ acceptor liposomes
donor + acceptor liposomes only
+ dithionite
NBD-fluorescence (a.u.)
20
40
60
80
100
Time (mins)
G
SHIP164 dimer
MBP-SHIP164 dimer
10 nm
H
10 nm
I
120°
~100 Å

Figure 1

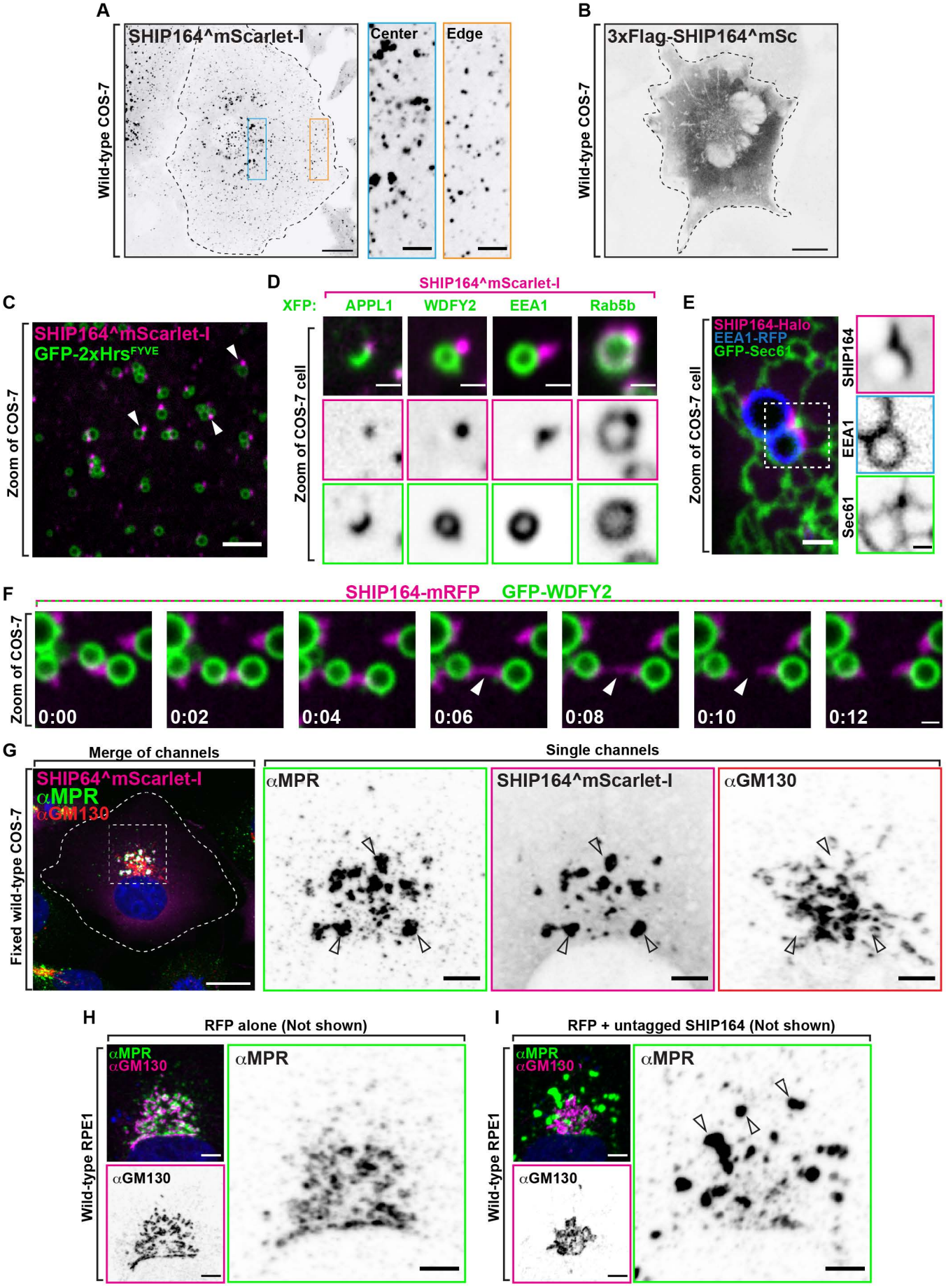
A
SHIP164^mScarlet-I
Center
Edge
Wild-type COS-7
B
3xFlag-SHIP164^mSc
Wild-type COS-7
C
SHIP164^mScarlet-I
GFP-2xHrsFYVE
Zoom of COS-7
D
SHIP164^mScarlet-I
XFP:
APPL1
WDFY2
EEA1
Rab5b
Zoom of COS-7 cell
E
SHIP164-Halo
EEA1-RFP
GFP-Sec61
Zoom of COS-7 cell
SHIP164
EEA1
Sec61
F
SHIP164-mRFP
GFP-WDFY2
Zoom of COS-7
0:00
0:02
0:04
0:06
0:08
0:10
0:12
G
Merge of channels
Single channels
SHIP64^mScarlet-I
αMPR
αGM130
Fixed wild-type COS-7
αMPR
SHIP164^mScarlet-I
αGM130
H
RFP alone (Not shown)
αMPR
αGM130
Wild-type RPE1
αMPR
αGM130
I
RFP + untagged SHIP164 (Not shown)
αMPR
αGM130
Wild-type RPE1
αMPR
αGM130

Figure 2

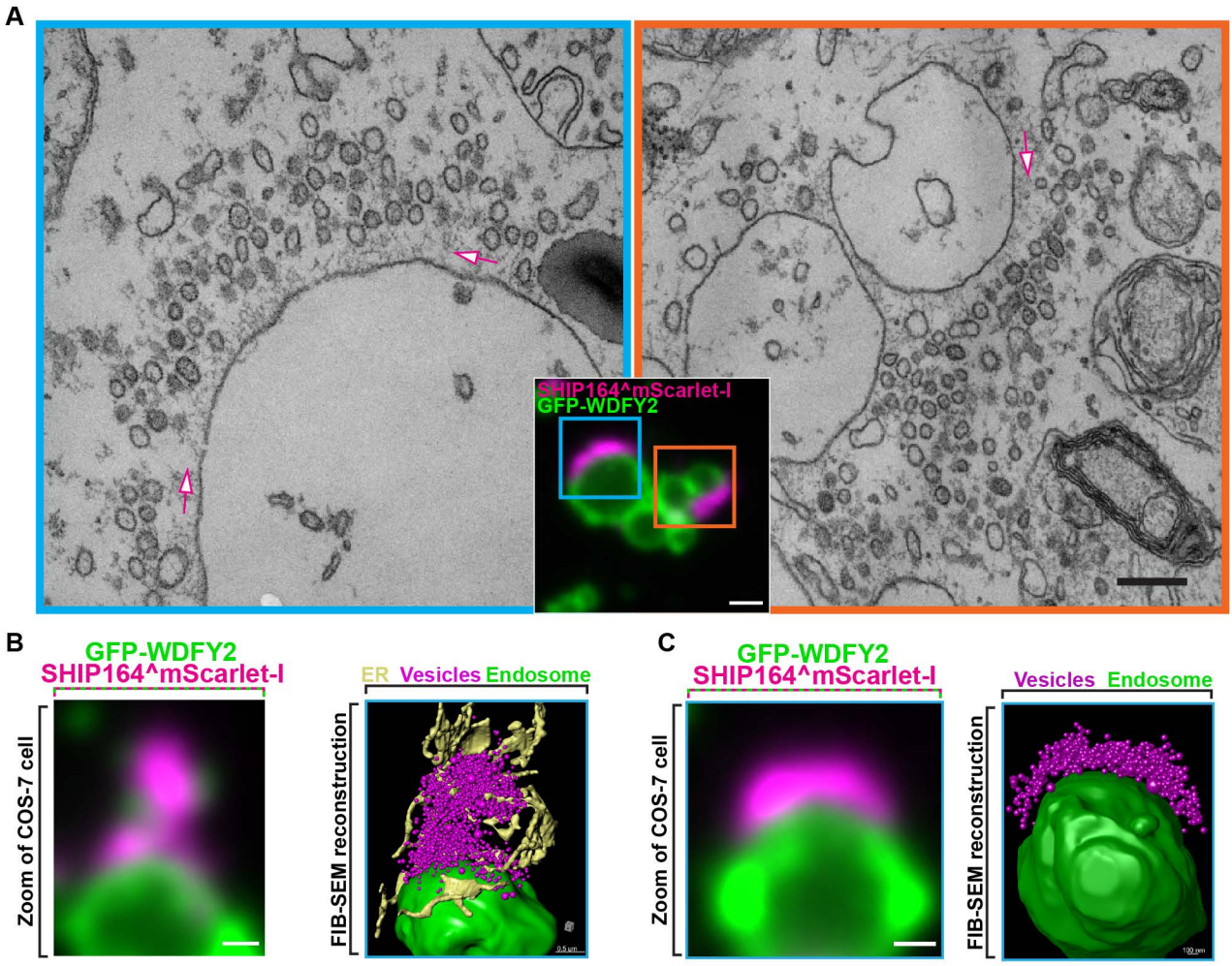
A
SHIP164^mScarlet-I
GFP-WDFY2
B
GFP-WDFY2
SHIP164^mScarlet-I
Zoom of COS-7 cell
ER
Vesicles
Endosome
FIB-SEM reconstruction
C
GFP-WDFY2
SHIP164^mScarlet-I
Zoom of COS-7 cell
Vesicles
Endosome
FIB-SEM reconstruction

Figure 3

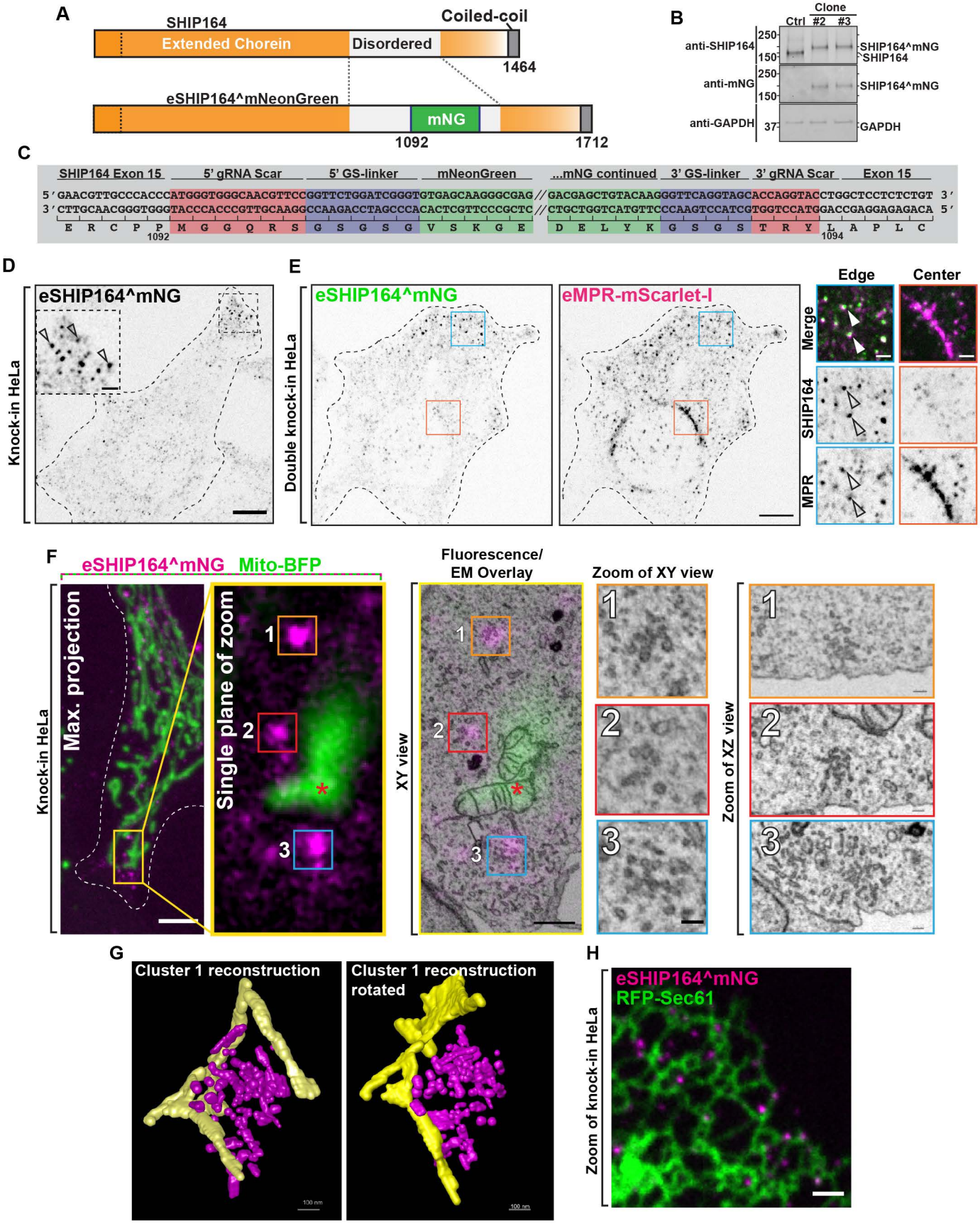
A
SHIP164
Extended Chorein
Disordered
Coiled-coil
1464
eSHIP164^mNeonGreen
mNG
1092
1712
B
Clone
Ctrl #2 #3
anti-SHIP164
250
150
SHIP164^mNG
SHIP164
anti-mNG
250
150
SHIP164^mNG
anti-GAPDH
37
GAPDH
C
SHIP164 Exon 15
5' gRNA Scar
5' GS-linker
mNeonGreen
...mNG continued
3' GS-linker
3' gRNA Scar
Exon 15
5' GAACGTTGCCCACCCATGGGTGGGCAACGTTCCGGTTCTGGATCGGGTGTGAGCAAGGGCGAG // GACGAGCTGTACAAGGGTTCAGGTAGCACCAGGTACCTGGCTCCTCTCTGT 3'
3' CTTGCAACGGGTGGGTACCCACCCGTTGCAAGGCCAAGACCTAGCCCACACTCGTTCCCGCTC // CTGCTGGTCATGTTCCCAAGTCCATCGTGGTCCATGGACCGAGGAGAGACA 5'
E R C P P M G G Q R S G S G S G V S K G E
1092
D E L Y K G S G S T R Y L A P L C
1094
D
Knock-in HeLa
eSHIP164^mNG
E
Double knock-in HeLa
eSHIP164^mNG
eMPR-mScarlet-I
Edge
Center
Merge
SHIP164
MPR
F
eSHIP164^mNG
Mito-BFP
Knock-in HeLa
Max. projection
Single plane of zoom
1
2
3
Fluorescence/
EM Overlay
XY view
Zoom of XY view
Zoom of XZ view
G
Cluster 1 reconstruction
Cluster 1 reconstruction
rotated
100 nm
H
Zoom of knock-in HeLa
eSHIP164^mNG
RFP-Sec61

Figure 4

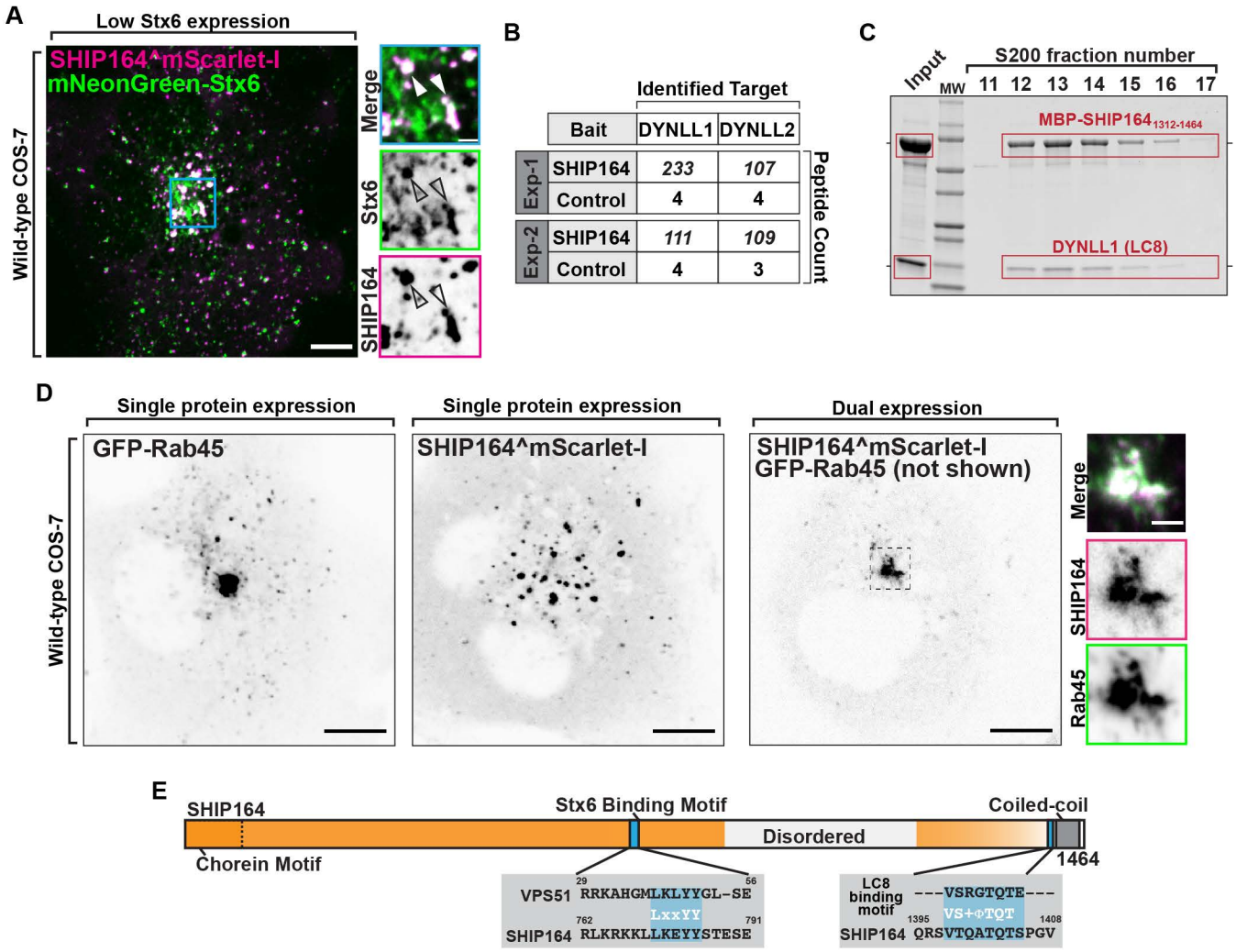
A
Low Stx6 expression
Wild-type COS-7
SHIP164^mScarlet-I
mNeonGreen-Stx6
Merge
Stx6
SHIP164
B
Identified Target
Bait
DYNLL1
DYNLL2
Exp-1
SHIP164
233
107
Control
4
4
Exp-2
SHIP164
111
109
Control
4
3
Peptide Count
C
Input
MW
S200 fraction number
11 12 13 14 15 16 17
MBP-SHIP164 1312-1464
DYNLL1 (LC8)
D
Single protein expression
Single protein expression
Dual expression
Wild-type COS-7
GFP-Rab45
SHIP164^mScarlet-I
SHIP164^mScarlet-I
GFP-Rab45 (not shown)
Merge
SHIP164
Rab45
E
SHIP164
Stx6 Binding Motif
Coiled-coil
Disordered
Chorein Motif
1464
VPS51 RRKAHGMLKLYYGL-SE
LxxYY
SHIP164 RLKRKKLLKEYYSTESE
LC8 binding motif
---VSRGTQTE---
VS+ΦTQT
SHIP164 QRSVTQATQTSPGV

Figure 5

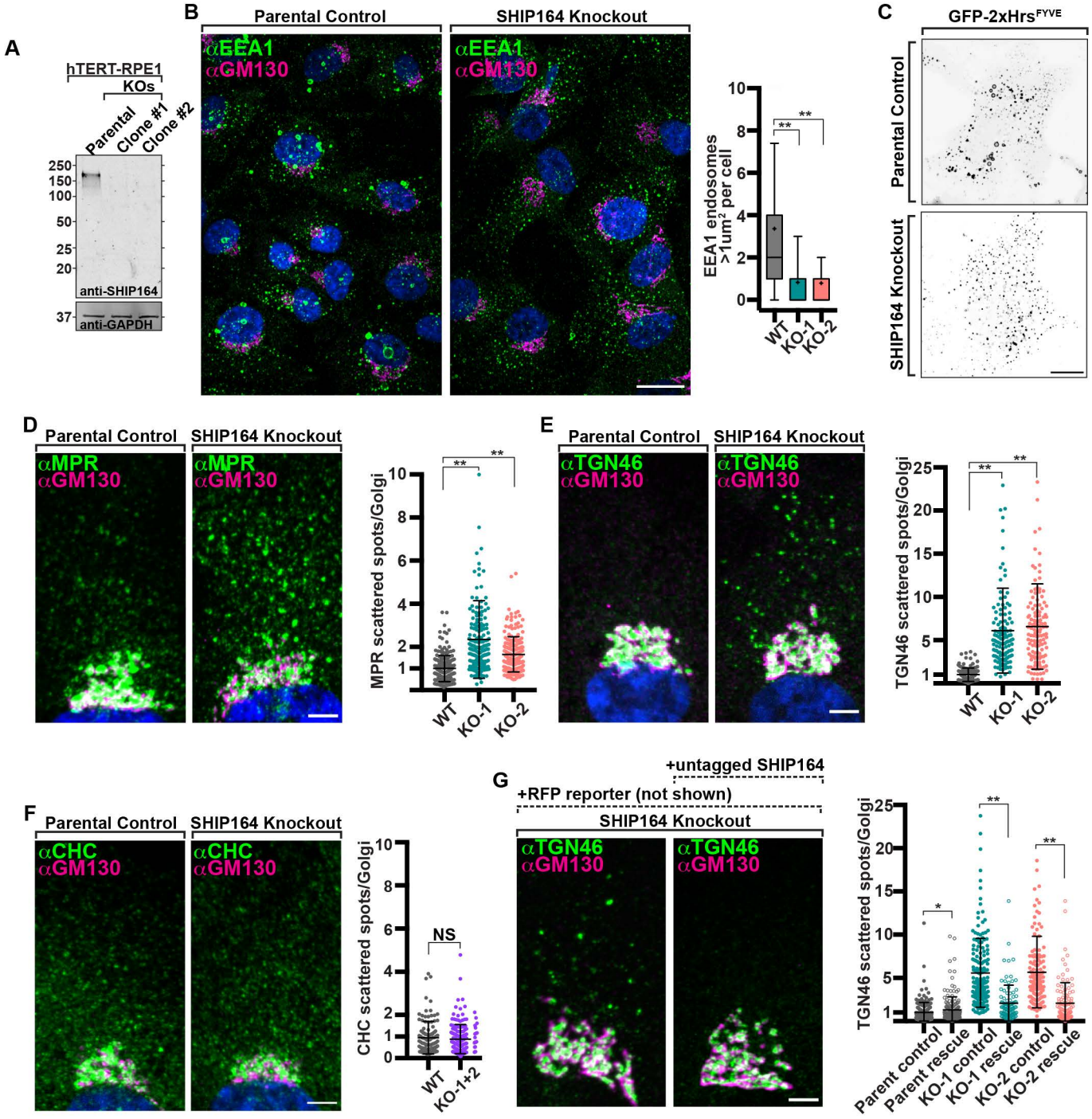
A
hTERT-RPE1
KOs
Parental
Clone #1
Clone #2
250
150
100
50
25
20
anti-SHIP164
37
anti-GAPDH
B
Parental Control
SHIP164 Knockout
αEEA1
αGM130
EEA1 endosomes >1um² per cell
WT
KO-1
KO-2
C
GFP-2xHrsFYVE
Parental Control
SHIP164 Knockout
D
Parental Control
SHIP164 Knockout
αMPR
αGM130
MPR scattered spots/Golgi
E
αTGN46
TGN46 scattered spots/Golgi
F
αCHC
CHC scattered spots/Golgi
NS
WT
KO-1+2
G
+untagged SHIP164
+RFP reporter (not shown)
Parent control
Parent rescue
KO-1 control
KO-1 rescue
KO-2 control
KO-2 rescue

Figure 6

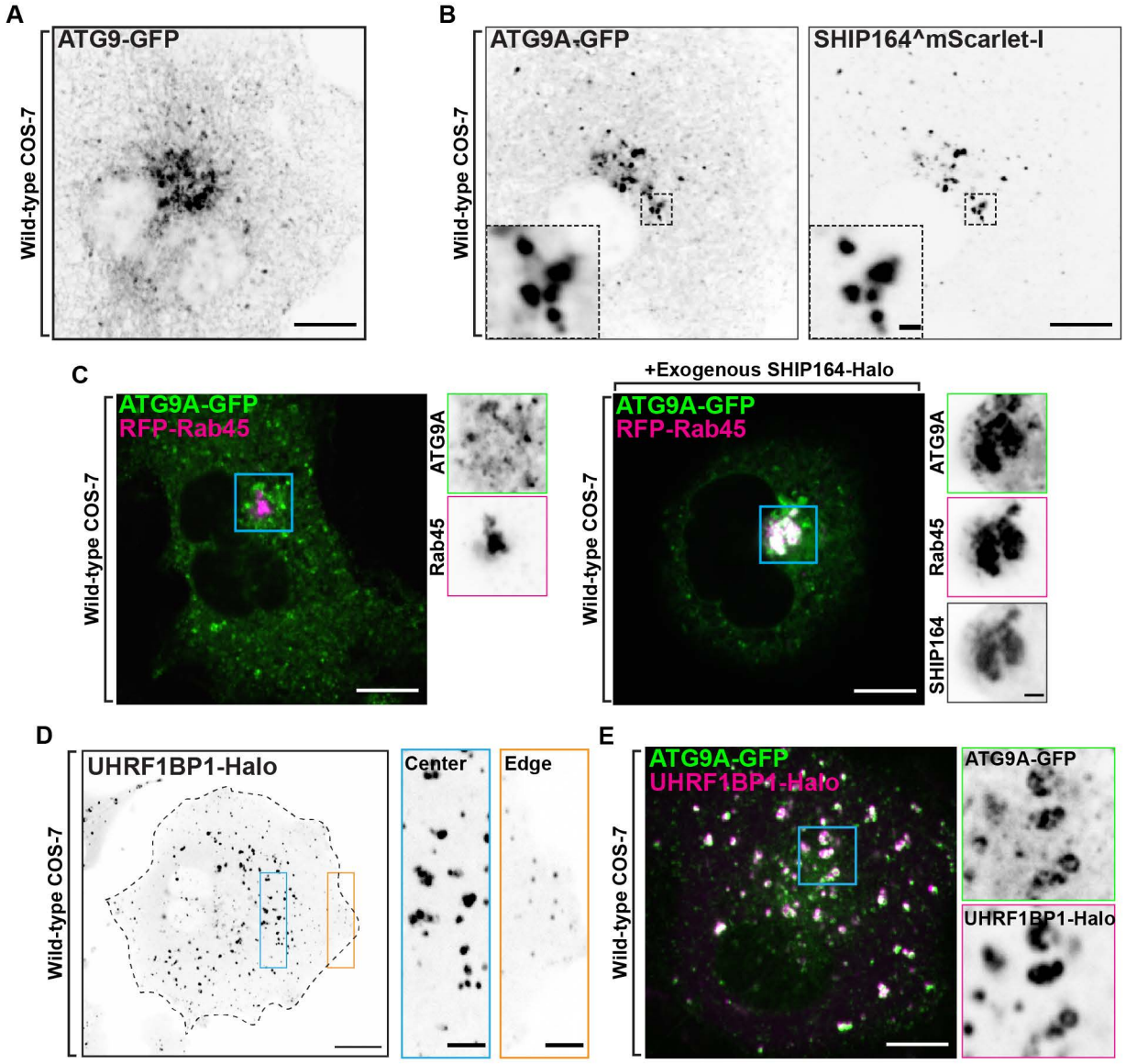
A
ATG9-GFP
Wild-type COS-7
B
ATG9A-GFP
SHIP164^mScarlet-I
Wild-type COS-7
C
ATG9A-GFP
RFP-Rab45
Wild-type COS-7
ATG9A
Rab45
+Exogenous SHIP164-Halo
ATG9A-GFP
RFP-Rab45
Wild-type COS-7
ATG9A
Rab45
SHIP164
D
UHRF1BP1-Halo
Wild-type COS-7
Center
Edge
E
ATG9A-GFP
UHRF1BP1-Halo
Wild-type COS-7
ATG9A-GFP
UHRF1BP1-Halo

Figure 7

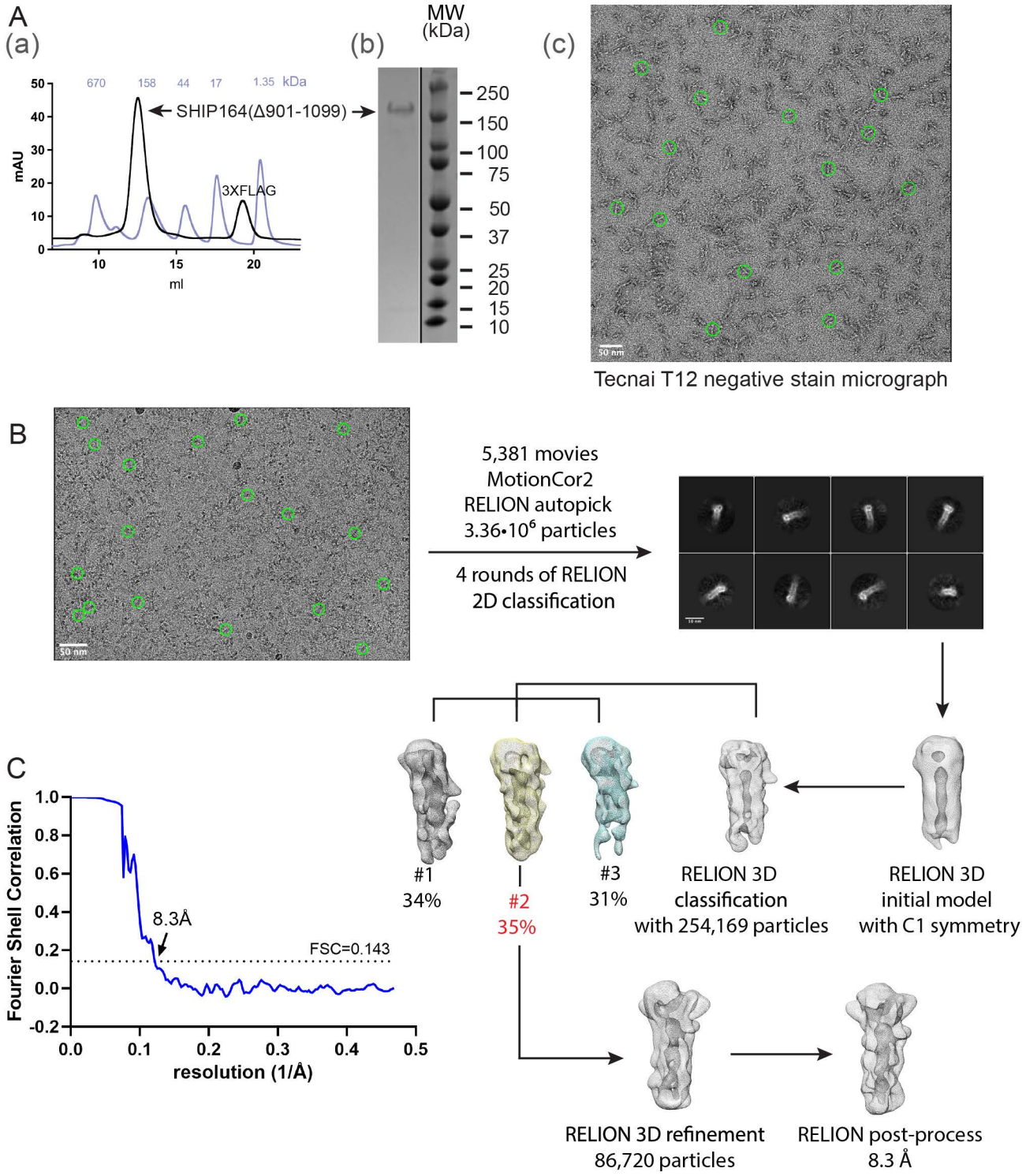

Supplemental Figure 1

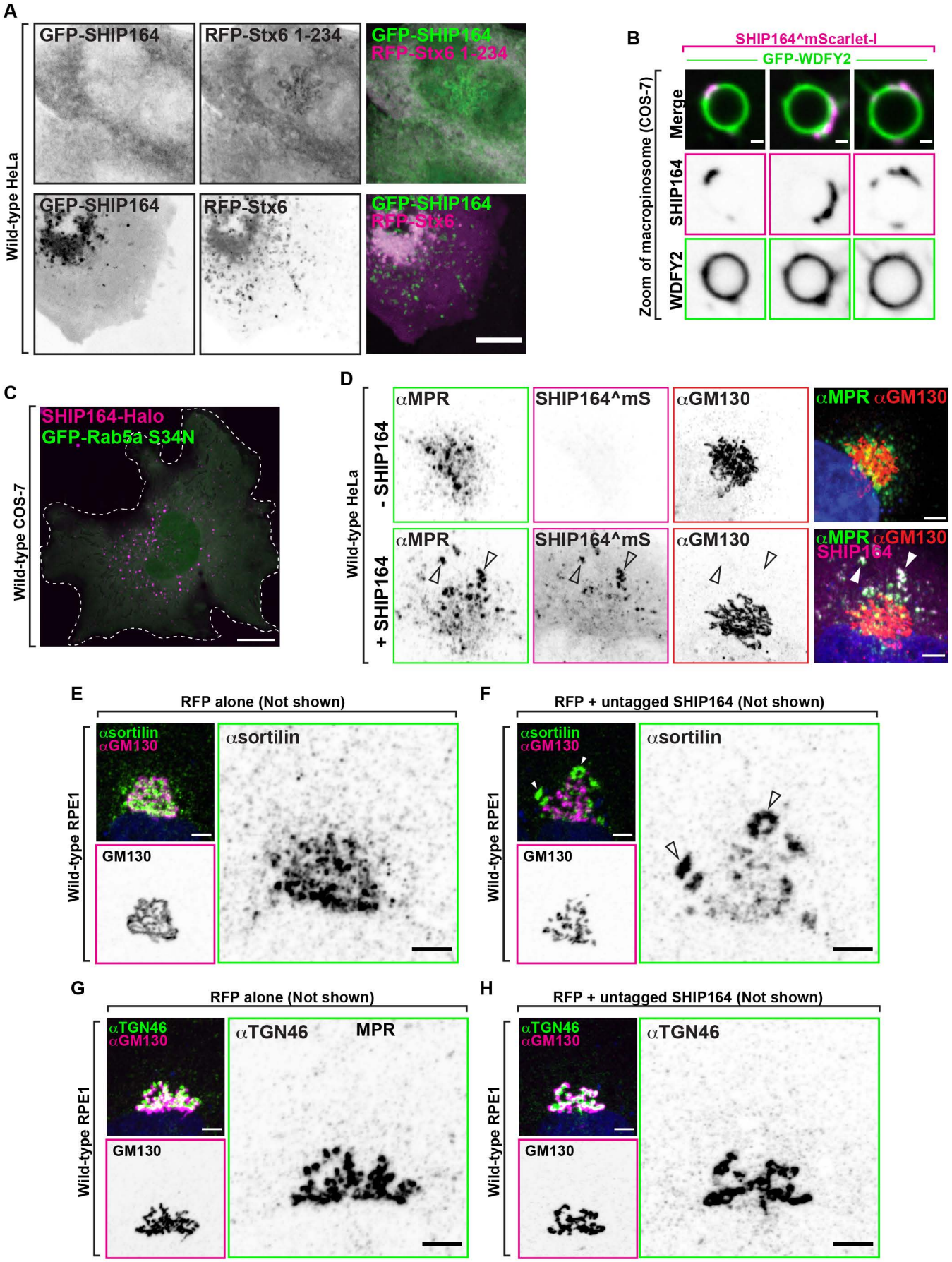

Supplemental Figure 2

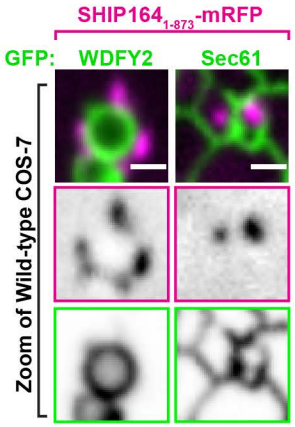

Supplemental Figure 3

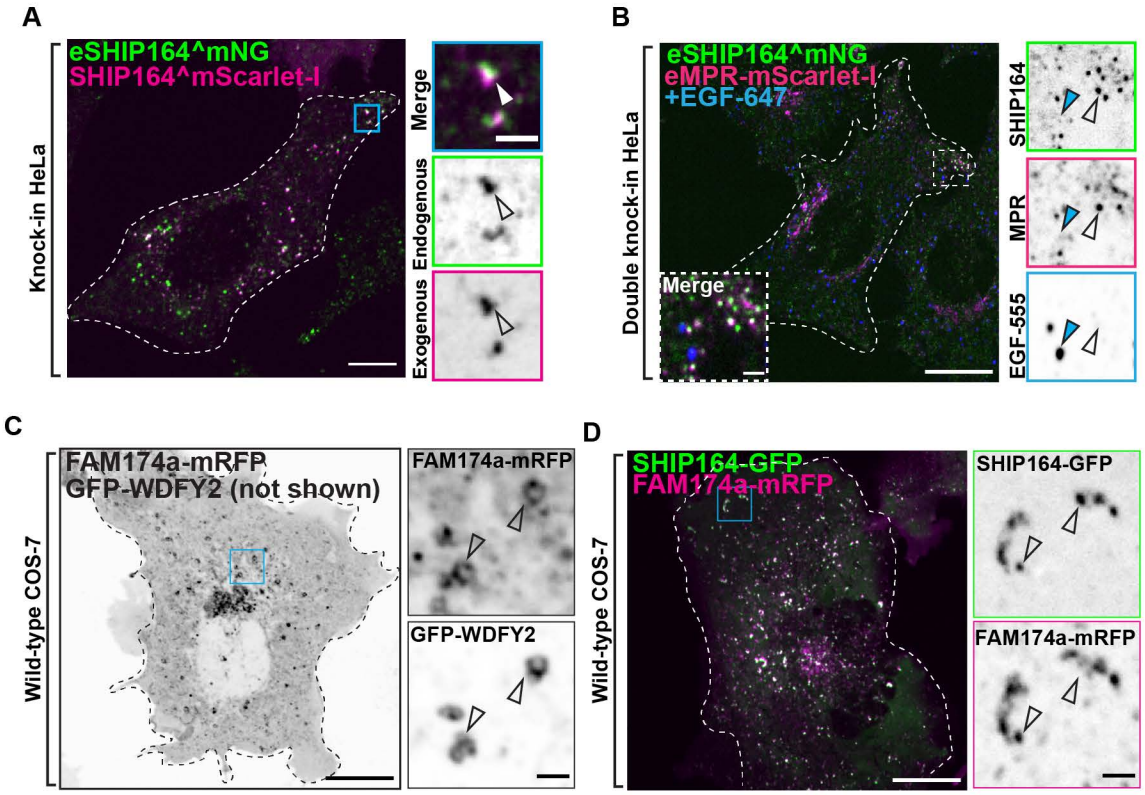

Supplemental Figure 4

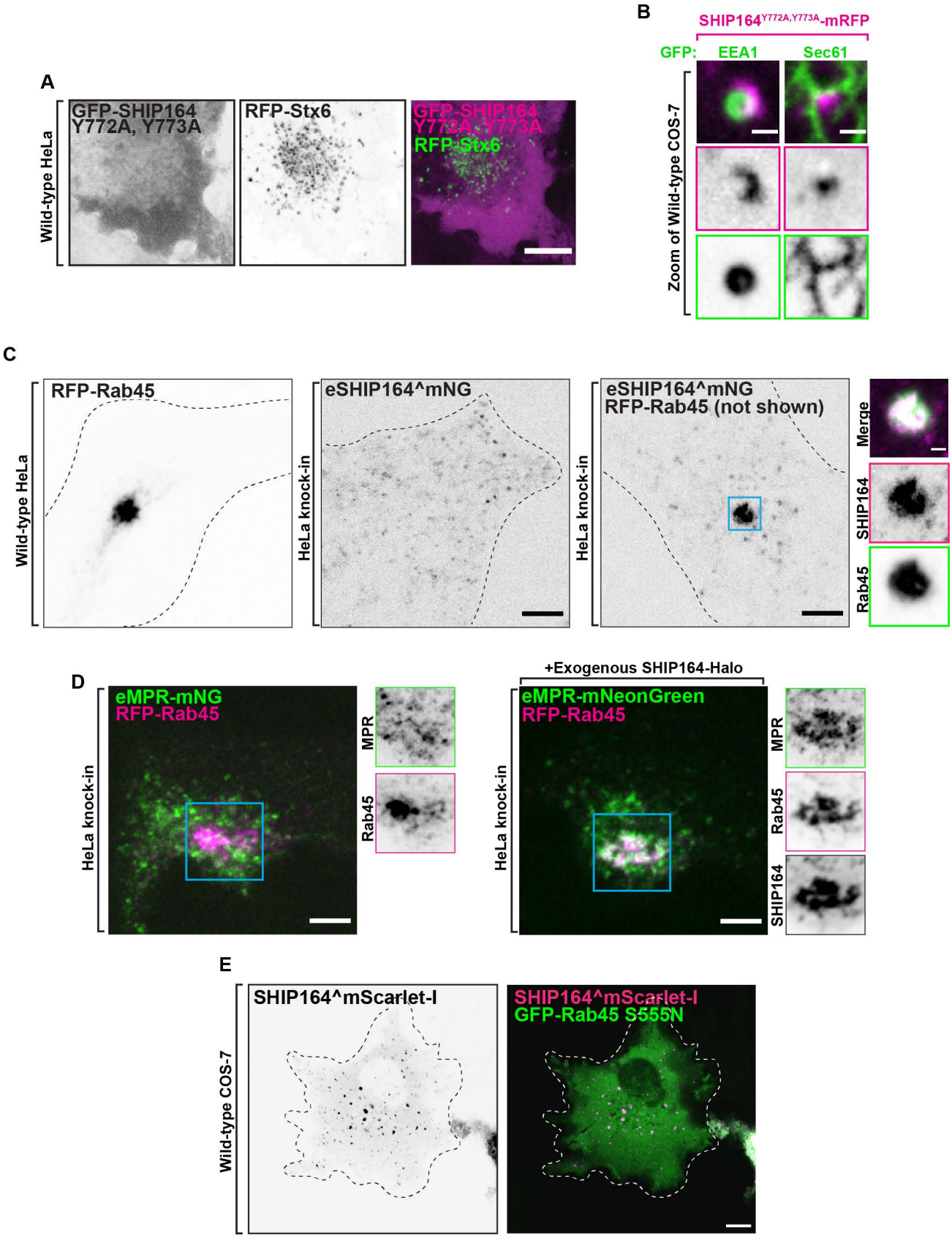

Supplemental Figure 5

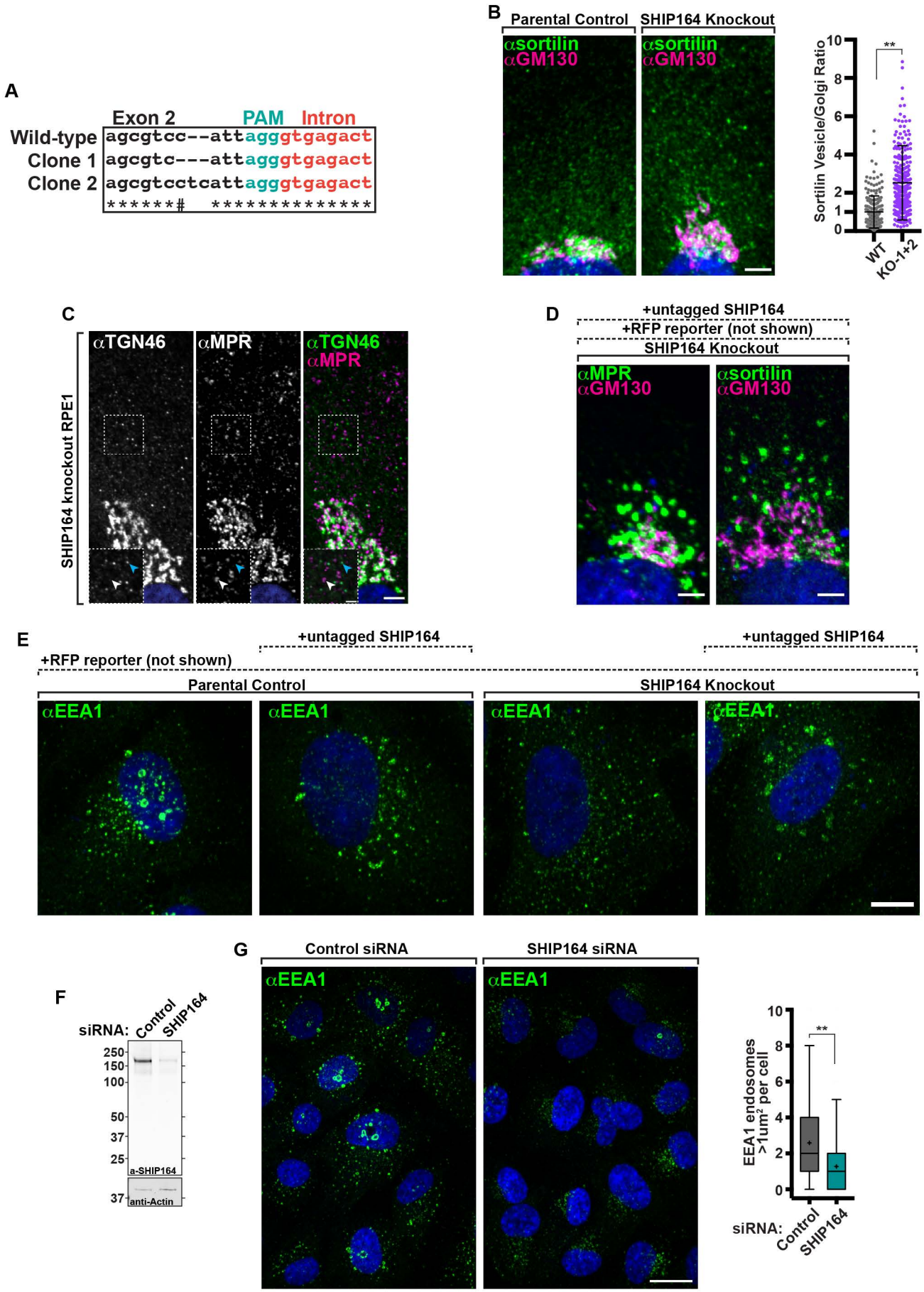

Supplemental Figure 6

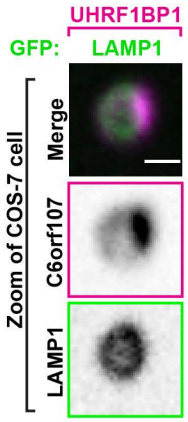

Supplemental Figure 7